On the phosphors $Na_5M(WO_4)_4$ (M = Y, La–Nd, Sm–Lu, Bi) – crystal structures, thermal decomposition, and optical and magnetic properties†

Matthias Hämmer,[a] Oliver Janka,[b,c] Judith Bönnighausen,[b] Steffen Klenner,[b] Rainer Pöttgen[b] and Henning A. Höppe*[a]

The pentasodium rare-earth tungstates $Na_5M(WO_4)_4$ are closely related to the sodium rare-earth double tungstates $Na_5M(WO_4)_2$ both adopting the *scheelite* structure type (space group $I4_1/a$, no. 88). After the preparation of polycrystalline powders *via* flux syntheses improving the phase purity significantly, the crystal structures of $Na_5M(WO_4)_4$ (M = Y, La–Nd, Sm–Lu, Bi) were determined by single crystal XRD and Rietveld analysis. $Na_5M(WO_4)_4$ is a promising phosphor material both as a host and as a 100% phosphor due to the possible charge transfer of the tungstate group and the absence of any concentration quenching. $Na_5M(WO_4)_4$ incongruently melts to $Na_5M(WO_4)_2$ and Na_2WO_4. After the clarification of the crystallographic relationship of $Na_5M(WO_4)_4$ and $Na_5M(WO_4)_2$ based on a rare isomorphic transition of index 5 (*i*5) the non-linear trend of the decomposition temperature within the row of rare earth ions is explained systematically taking into account the existence of domains within the crystal structure predetermining the posterior decomposition. A miscibility gap for solid solutions of $Na_5Y(WO_4)_4$ and $Na_5Eu(WO_4)_4$ or $Na_5Tb(WO_4)_4$ is identified and its temperature dependence is investigated. Furthermore, the investigation of the fluorescent properties of $Na_5M(WO_4)_4$ (M = Pr, Sm, Eu, Tb, Tm, Bi), $Na_5Y_{1-x}Eu_x(WO_4)_4$ and $Na_5Y_{1-y}Tb_y(WO_4)_4$ provided insights into the weak ligand field and the energy transfer from WO_4^{2-} to M^{3+} governed by the emission of the sensitiser within $Na_5M(WO_4)_4$. Additionally, the compounds were characterised by magnetic measurements and vibrational, UV/Vis and ^{151}Eu Mössbauer spectroscopy.

Introduction

Tungstates are capable of forming WO_4 tetrahedra—besides WO_6 octahedra and WO_5 moieties[1–18]—and can therefore be classified as silicate-analogous materials like, *e.g.*, borosulfates,[19,20] fluorooxoborates[21,22] and polyphosphates.[23,24] Silicate-analogous materials comprise tetrahedral basic building units as the characteristic structural motif. The absence of an inversion centre within these tetrahedra often leads to interesting optical properties as they foster non-centrosymmetric coordination environments around emitting cations and thus promote high luminescence probabilities. The first systematic report on pentasodium rare earth tetratungstates $Na_5M(WO_4)_4$ dates back over 70 years.[25] The $Na_5M(WO_4)_4$ representations crystallise isomorphously across the lanthanide series closely related to scheelite in the space group $I4_1/a$ (no. 88) with the tungstate forming tetrahedral WO_4^{2-} units.[26–31] $Na_5M(WO_4)_4$ is reported to be a promising phosphor material both as a host and as a 100% phosphor because of its high chemical and thermal stability, low synthesis temperatures and lack of concentration quenching due to the special structural arrangement of M–O–W–O–M resulting in large M–M distances and consequently inhibition of energy transfer between M^{3+} ions.[30,32–36] Such phosphors may be of importance for the development of efficient luminescent devices like white LEDs or lamps.[37–39] Moreover, an important feature of tungstate phosphors is the antenna effect for which the tungstate acts as an efficient sensitiser transferring energy onto the activator. A ligand to metal charge transfer (LMCT) of O^{2-}–W^{6+} can frequently be excited by UV radiation subsequently enhancing forbidden f–f transition emissions of the rare earth ions *via* energy transfer.[3,4,40,41] Through the absorption of photons within the WO_4^{2-} group, electrons from the 2p states of O^{2-} are excited to the 5d states of W^{6+}, *e.g.* from the ground state W^{6+}–O^{2-} to the excited state W^{5+}–O^{-}.[40,42]

---

[a] *Lehrstuhl für Festkörperchemie, Universität Augsburg, Universitätsstraße 1, 86159 Augsburg, Germany. E-mail: henning.hoeppe@physik.uni-augsburg.de*

[b] *Institut für Anorganische und Analytische Chemie, Universität Münster, Corrensstrasse 30, 48149 Münster, Germany*

[c] *Universität des Saarlandes, Anorganische Festkörperchemie, Campus C4 1, 66123 Saarbrücken, Germany*

† Electronic supplementary information (ESI) available. CSD 1986858–1986876. For ESI and crystallographic data in CIF or other electronic format see DOI: 10.1039/D0DT00782J

At temperatures between 620 and 750 °C, $Na_5M(WO_4)_4$ melts simultaneously with the decomposition of the material[5,35,43,44] according to the reaction equation

$$Na_5M(WO_4)_4 \rightarrow 2Na_2WO_4 + NaM(WO_4)_2.$$

The competition between $Na_5M(WO_4)_4$ and $NaM(WO_4)_2$ – both crystallising in the space group $I4_1/a$ (ref. 5, 45–47) – is also responsible for the observation that there are almost no reports on $A_5M(WO_4)_4$ with A = Li or K.[6,26] In general, the material classes $Na_5M(WO_4)_4$ and $Na_5M(MoO_4)_4$ as well as $NaM(WO_4)_2$ and $NaM(MoO_4)_2$ are isotypic.[27,32,33,46,47]

In this contribution, the whole range of $Na_5M(WO_4)_4$ (M = La–Nd, Sm–Lu, Y, Bi) was prepared *via* flux syntheses significantly improving the purity of the obtained phosphor compared to solid state syntheses reported in the literature.[6,30,36] We apply single crystal X-ray diffraction (XRD) and Rietveld analysis for crystal structure determination for the purpose of the first systematic comparison over the whole range of rare earth ions. The crystal structure discussion is supported by electrostatic calculations. Furthermore, the crystallographic relationship between $Na_5M(WO_4)_4$ and $NaM(WO_4)_2$ is examined in detail in order to find a group–subgroup relation according to the Bärnighausen formalism.[48,49] Thereafter, the decomposition is investigated searching for a trend throughout the rare earth ions. Moreover, the $Na_5M(WO_4)_4$ compounds are investigated by infrared, UV/Vis, fluorescence and ^{151}Eu Mössbauer spectroscopy with special interest in the energy transfer mechanism from the LMCT O^{2-}–W^{6+} to the M^{3+} activator as well as for their magnetic properties in order to clarify the interaction of neighbouring M^{3+} ions; these will be compared with the investigations on the magnetic properties of $Na_5Eu(WO_4)_4$ reported earlier.[50] Additionally, solid solutions of $Na_5Y_{1-x}Eu_x(WO_4)_4$ and $Na_5Y_{1-x}Tb_x(WO_4)_4$ are addressed using both Rietveld analysis and fluorescence spectroscopy.

Results and discussion

Syntheses

Polycrystalline samples of $Na_5M(WO_4)_4$ (M = La–Nd, Sm–Lu, Y, Bi) were prepared at 600 °C *via* flux syntheses with an excess of 500% of the educt $Na_2WO_4 \cdot 2H_2O$ and checked by powder XRD for phase purity (Fig. 1). The excess educt facilitates the formation of $Na_5M(WO_4)_4$ over the competitive $NaM(WO_4)_2$, while the leftover Na_2WO_4 is water soluble[9,11,31] and consequently washed out during the further synthesis process. Nevertheless, a side phase of $NaM(WO_4)_2$ of, *e.g.*, 2 wt% $NaEu(WO_4)_2$ in $Na_5Eu(WO_4)_4$ could be found by Rietveld refinement (Fig. S1 in the ESI†). The formation of this side phase is apparently significantly suppressed as solid state syntheses at the same temperature of 600 °C (Synthesis A1) as well as at 700 °C (Synthesis A2) yield major $NaEu(WO_4)_2$ side phase amounts of 17 wt% and 16 wt% according to Rietveld refinements, respectively (Fig. S2†).

Starting from the polycrystalline samples, single crystals of $Na_5M(WO_4)_4$ (M = Ce, Pr, Nd, Sm, Eu, Gd, Tb, Ho, Tm, Yb, Bi) were obtained *via* recrystallisation from the melt. Consequently, we performed single-crystal X-ray structure determinations on $Na_5M(WO_4)_4$ (M = Ce–Nd, Sm–Tb, Ho, Tm, Yb, Bi) (Tables 1, S1 and S2†) along with Rietveld refinements of $Na_5M(WO_4)_4$ (M = La, Pr, Sm–Lu, Y) (Tables S3 and S4, Fig. S3 and S4†) accompanied by further characterisation.

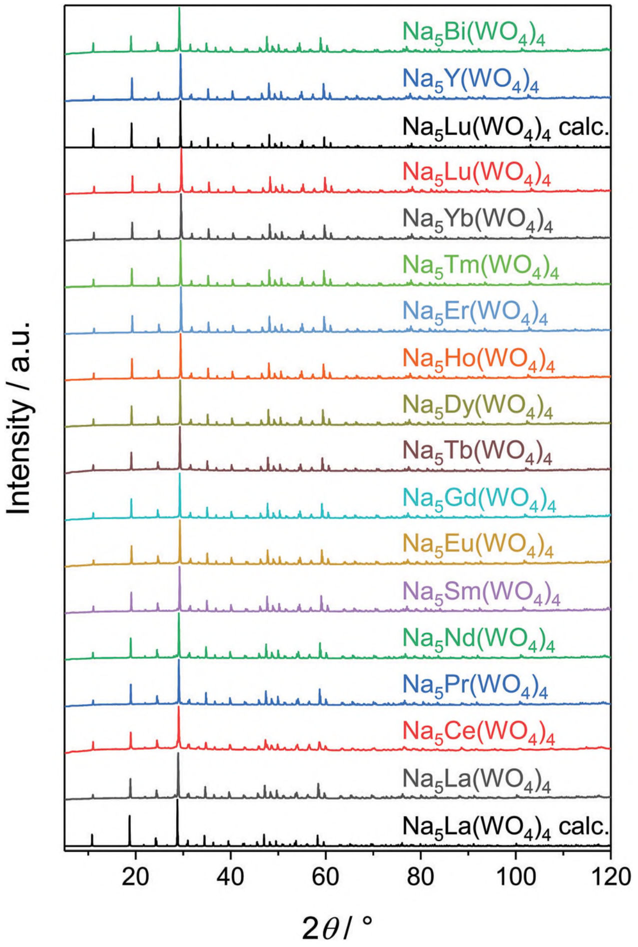

Fig. 1 Powder XRD patterns of polycrystalline $Na_5M(WO_4)_4$ (M = La–Nd, Sm–Lu, Y, Bi) compared to patterns calculated from the results of the Rietveld refinement of $Na_5La(WO_4)_4$ and $Na_5Lu(WO_4)_4$ (see Tables S3 and S4†).

Samples of $Na_5Y_{1-x}Eu_x(WO_4)_4$ (x = 0.01, 0.05, 0.1, 0.5) and $Na_5Y_{1-y}Tb_y(WO_4)_4$ (y = 0.01, 0.02, 0.05, 0.5) were synthesised in order to study the fluorescent properties. For the samples $Na_5Y_{0.5}Eu_{0.5}(WO_4)_4$ and $Na_5Y_{0.5}Tb_{0.5}(WO_4)_4$ we identified a temperature dependent miscibility gap for solid solutions of $Na_5Y(WO_4)_4$ and $Na_5Eu(WO_4)_4$ or $Na_5Tb(WO_4)_4$, respectively. Consequently, single crystals of $Na_5Y_{0.5}Eu_{0.5}(WO_4)_4$ and $Na_5Y_{0.5}Tb_{0.5}(WO_4)_4$ were grown from the melt starting from the polycrystalline powders and single-crystal X-ray structure determination was performed along with Rietveld refinements. Additionally, $Na_5Y_{0.5}Eu_{0.5}(WO_4)_4$ samples were prepared *via* two different solid state syntheses A1 and A2 and analysed by Rietveld analysis, while the closing of the miscibility gap was investigated by variable temperature powder XRD on $Na_5Y_{0.5}Eu_{0.5}(WO_4)_4$ prepared by flux synthesis.

Furthermore, phase pure polycrystalline $NaEu(WO_4)_2$ was synthesised *via* a solid state reaction (Fig. S5†) and starting

Table 1 Crystal data and structure refinements of $NaEu(WO_4)_2$ and $Na_5Eu(WO_4)_4$ determined from single-crystal data (the respective standard deviations are given in parentheses)

	$NaEu(WO_4)_2$	$Na_5Eu(WO_4)_4$
M/g mol^{-1}	670.65	1258.31
Crystal size/mm^3	0.04 × 0.04 × 0.03	0.10 × 0.06 × 0.03
Temperature/K	298(2)	301(2)
Space group	$I4_1/a$	$I4_1/a$
a/pm	526.24(1)	1149.98(4)
c/pm	1140.78(3)	1140.61(4)
Volume/10^6 pm^3	316.07(3)	1508.40(12)
Z	2	4
ρ_{calcd}/g cm^{-3}	7.05	5.54
Absorption coefficient μ/mm^{-1}	46.2	34.7
F(000)/e	572	2168
Radiation; wavelength λ/Å	MoKα; 0.71073	MoKα; 0.71073
Diffractometer	Bruker D8 Venture	Bruker D8 Venture
Absorption correction	Multi-scan	Multi-scan
Transmission (min; max)	0.6338; 0.7503	0.6001; 0.7483
Index range $h\|k\|l$	−9/19|−9/9|−21/21	−20/20|−15/20|−20/20
θ range/°	4.265–41.863	2.515–39.996
Reflections collected	21 433	16 901
Independent reflections	546	2337
R_{int}	0.0284	0.0406
Obs. reflections ($I > 2\sigma(I)$)	472	2025
Refined parameters	16	60
R_1 (all data)	0.018	0.0258
wR_2 (all data)	0.034	0.0356
GooF	1.12	1.026
Residual electron density (max; min)/e$^-$ Å^{-3}	2.08; −1.51	1.41; −1.18

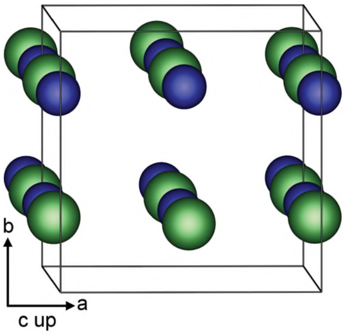

Fig. 2 Na/Eu–W chains along the c axis in $NaEu(WO_4)_2$ displayed together with the unit cell (Na/Eu green, W blue).

from this, single crystals were grown from the melt. Single-crystal X-ray structure determination was performed enabling an adequate comparison of the concurring and crystallographically closely related structures of $NaEu(WO_4)_2$ and $Na_5Eu(WO_4)_4$ (Table 1).

Crystal structures

$NaEu(WO_4)_2$. $NaEu(WO_4)_2$ adopts the scheelite structure type ($CaWO_4$) in the space group $I4_1/a$ (no. 88) with one half of the Ca^{2+} positions occupied by Na^+ and the remaining ones by Eu^{3+}.[5,45–47] The refinement of single-crystal XRD data yielded a mixed occupation of 51.8(2)% Na and 48.2(2)% Eu in our structure model over the same 4b site. The details are presented in Table 1. The tungsten atom on the Wyckoff position 4a is coordinated by four oxygen atoms forming non-condensed WO_4 tetrahedra which are connected *via* corners to distorted $[(Na/Eu)O_8]$ dodecahedra with four oxygen atoms coordinating with a distance of 245.7(2) pm and the other four with a distance of 247.7(2) pm (see Table S5 and Fig. S6†). These values are reasonably close to the sum of the respective ionic radii (248 pm).[51] The same holds for the W–O interactions with the W–O distance of 179.0(2) pm (sum of ionic radii 178 pm).[51] The $[(Na/Eu)O_8]$ dodecahedra are connected to adjacent ones *via* edges. The cations Na^+/Eu^{3+} and W^{6+} form Na/Eu–W chains along the c axis (Fig. 2). According to the calculation of the deviation from the ideal symmetry Δ_{tetr} by the method of Balic-Zunic and Makovicky[52,53] the WO_4 tetrahedra can be classified as regular (Δ_{tetr} = 0.53%).[24]

$Na_5M(WO_4)_4$ (M = La–Nd, Sm–Lu, Y, Bi). All compounds of the $Na_5M(WO_4)_4$ series crystallise in a *scheelite* related structure in the space group $I4_1/a$ (no. 88).[5,26,27,33,46] The details of the structure determinations are presented in Tables 1, S1–S4, Fig. S1, S3 and S4.† The unit cell (see Fig. S7†) comprises non-condensed WO_4 tetrahedra. They consist of four crystallographically distinct sites O1, O2, O3 and O4. Non-condensed MO_8 dodecahadra including two groups of crystallographically equivalent M–O distances of, *e.g.*, 240.3(2) pm and 240.7(2) pm for $Na_5Eu(WO_4)_4$ (sum of ionic radii 242.6 pm (ref. 51)) are located on the special position 4a on the $\bar{4}$ axis. WO_4 and MO_8 are connected *via* corners setting up a network $^3_\infty\left[M(WO_4)_{\frac{4}{5}}\right]^{5-}$. The resulting cavities are filled with Na^+ located on two non-equivalent lattice sites. Distorted $Na(1)O_6$ trigonal prisms on the special Wyckoff site 4b are surrounded by six WO_4 tetrahedra *via* shared corners; distorted $Na(2)O_4$ tetrahedra are coordinated by eight $Na(1)O_6$ and four WO_4.[5,26,27,33] The respective cation environments are shown in Fig. S8.† Along the c axis, infinite W–Na(1) and M–Na(2) chains are formed (Fig. 3).

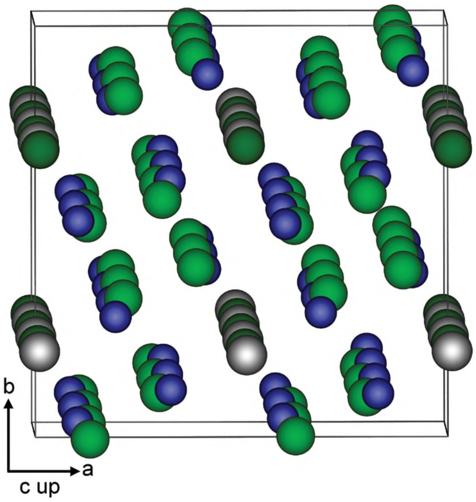

Fig. 3 Infinite W–Na(1) and M–Na(2) chains along the c axis in $Na_5M(WO_4)_4$ displayed together with the unit cell (blue W, green Na(1), dark green Na(2), grey M).

However, WO_4 tetrahedra and NaO_6 trigonal prisms as well as MO_8 dodecahedra and NaO_4 tetrahedra are not condensed along the W–Na(1) and M–Na(2) chains, respectively, but Na(1)O_6 is connected *via* edges to Na(1)O_6 and MO_8 and *via* corners to WO_4 and Na(2)O_4. Thus, the interconnection of neighbouring alternative chains forms the 3D framework. Consequently, the coordination numbers of the oxygen anions are four (O1) and three (O2, O3, O4).

Comparing all determined crystal structures for $Na_5M(WO_4)_4$ the lattice parameters *a* and *c* decrease with the ionic radii of M^{3+} following the lanthanide contraction (Fig. 4). This affects both axes equally due to the pseudocubic nature of $Na_5M(WO_4)_4$.[27] Additionally, the MO_8 dodecahedra adopt no special position towards the unit cell. Consequently, the lanthanide contraction resulting in shrinkage of the MO_8 dodecahedra affects both *a* and *c* evenly. According to Fig. 4, $Na_5Bi(WO_4)_4$ does not fit with the rare earth compounds' trend presumably since there are no f electrons in Bi^{3+}. Furthermore, Fig. 4 shows the matching of the lattice parameters determined from single crystal XRD and Rietveld data.

Tables S6–S9† show the selected interatomic distances and angles of $Na_5M(WO_4)_4$.‡ Again, the M–M and M–O distances decrease following the lanthanide contraction with the values of the latter reasonably close to the sum of the respective ionic radii.[51] The same holds for the Na–O and W–O distances. Both Na(1)–O and Na(2)–O distances decrease with the lanthanide contraction.

Again, the deviation of the WO_4 tetrahedra from tetrahedral symmetry Δ_{tetr} was calculated by the method of Balic-Zunic and Makovicky based on all ligands enclosing spheres on experimental data[52,53] (Tables S6–S9†).§ The results show a linear increase in the deviation with decreasing ionic radius and lanthanide contraction (Fig. S9†) in accordance with the report by Efremov *et al.* for $Na_5M(WO_4)_4$ (M = La, Tb, Lu).[27] However, the maximal deviation of 0.92% for $Na_5Yb(WO_4)_4$ is rather small. The tetrahedra can still be classified as regular.[24] The increase in deviation is linked to the unit cell decrease and the M–O distance decrease following the lanthanide contraction, whereas the W–O distances do not differ considerably (Tables S6–S9†). In contrast, the Na(2)O_4 tetrahedra are not regular with deviations of 7–8% (Tables S6–S9†).

On comparing $Na_5Bi(WO_4)_4$ with the other structures, no peculiarities in both the first and second coordination spheres of Bi^{3+} were found indicating an influence of the lone pair of Bi^{3+}. This is presumably due to the large Bi–Bi and Bi–O distances (see Table S9†). However, the lattice parameters *a* and *c* of the bismuth compound correspond to different rare earth compounds. *a* ranges between the figures of $Na_5Nd(WO_4)_4$ and $Na_5Sm(WO_4)_4$ while *c* corresponds to the values found for $Na_5Sm(WO_4)_4$ and $Na_5Eu(WO_4)_4$.

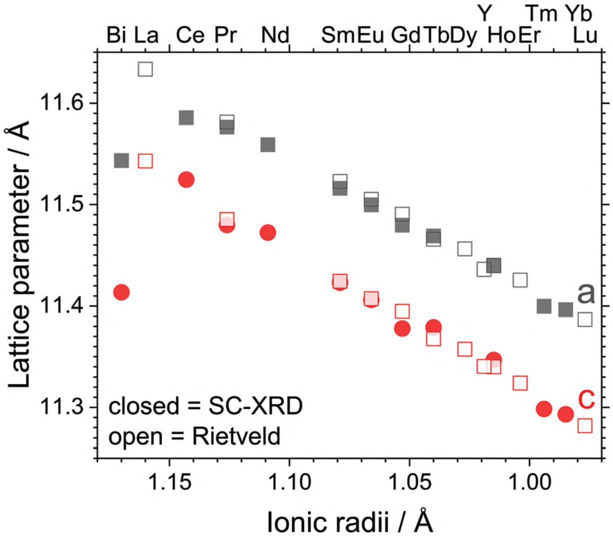

Fig. 4 The trend of the lattice parameters *a* and *c* with the ionic radii of M^{3+} in $Na_5M(WO_4)_4$: the open symbols indicate data from Rietveld refinement and the closed ones indicate data from single-crystal XRD; the graph shows the homogeneous decrease of both lattice parameters with the lanthanide contraction; on the very left, $Na_5Bi(WO_4)_4$ does not follow the trend due to Bi^{3+} not being part of the lanthanide series.

In the literature, the lack of concentration quenching in $Na_5M(WO_4)_4$ was attributed to the special structure M–O–W–O–M with angles of M–O–W of 110° or 100°.[30,35,36] Our data show that the M–O–W angle lies in fact around 130° for all studied compounds leaving the large M–M distances of 635 to 649 pm (Tables S6–S9†) as an obvious reason preventing energy transfer between M^{3+} ions and consequently reducing concentration quenching. These large distances are realised *via* double M–O–W–O–M bridges shown in Fig. 5; for $NaEu(WO_4)_2$ a quite short distance of only 388 pm is found (Table S5†).

In summary, the crystal structures of $Na_5M(WO_4)_4$ determined by single crystal XRD and Rietveld analysis of powder XRD data are in agreement with the earlier reports in the literature.[26–31] To the best of our knowledge, the first extensive reports of the structure are provided for $Na_5Ce(WO_4)_4$, $Na_5Pr(WO_4)_4$, $Na_5Sm(WO_4)_4$, $Na_5Dy(WO_4)_4$, $Na_5Ho(WO_4)_4$, $Na_5Er(WO_4)_4$, $Na_5Tm(WO_4)_4$, $Na_5Yb(WO_4)_4$ and $Na_5Bi(WO_4)_4$. Furthermore, we reported the first structure determinations of $NaEu(WO_4)_2$ and $Na_5Eu(WO_4)_4$ from single-crystal data.

Electrostatic calculations

The electrostatic reasonability of the crystal structures was confirmed by calculations based on the MAPLE concept (MAdelung Part of Lattice Energy).[54–56] The MAPLE values of $Na_5M(WO_4)_4$ (M = Pr, Sm, Eu, Tb, Ho, Yb, Bi) from single-crystal data and $Na_5M(WO_4)_4$ (M = La, Ho) from Rietveld data were calculated and compared with the sum of the respective

---

‡ In general, the determination of the exact bond distances from powder diffraction data is difficult due to the strong correlation of parameters. Therefore, it is somewhat daring to compare the structure models from Rietveld refinements with the ones based on single-crystal diffraction. However, the average values follow the trends. The calculation of the deviation of the polyhedra from the ideal symmetry based on Rietveld data was not reasonable due to the large margin of error of the bond distances. Where structure determination from both powder and single crystal data was performed, only the interatomic distances obtained by single crystal XRD were considered.

§ An implementation of this method into a script reading CIFs may be provided by the authors.

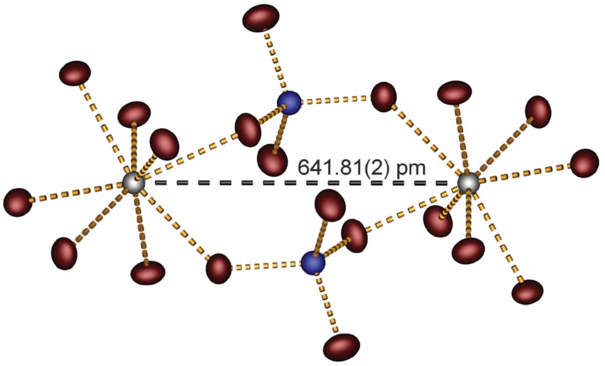

Fig. 5 The structural feature in $Na_5M(WO_4)_4$ (here M = Eu) showing the large Eu–Eu distances realised *via* Eu–O–W–O–Eu bridges; the ellipsoids of Eu^{3+} (grey), W^{6+} (blue) and oxygen (red) are shown at a 90% probability level.

Table 2 Electrostatic calculations for $NaEu(WO_4)_2$ and $Na_5M(WO_4)_4$ (M = Pr, Sm, Eu, Tb, Ho, Yb, Bi) from single-crystal data and $Na_5M(WO_4)_4$ (M = La, Ho) from Rietveld data

$NaEu(WO_4)_2$ (SC-XRD) MAPLE = 59 523 kJ mol^{-1}	$\frac{1}{2}Eu_2O_3$[57] + $2Na_2WO_4$[11] – $1.5Na_2O$[58] MAPLE = 59 555 kJ mol^{-1} (Δ = 0.05%)
$Na_5La(WO_4)_4$ (Rietveld) MAPLE = 115 590 kJ mol^{-1}	$\frac{1}{2}La_2O_3$[59] + $1.5WO_3$[60] + $2.5Na_2WO_4$[11] MAPLE = 116 583 kJ mol^{-1} (Δ = 0.86%)
$Na_5Pr(WO_4)_4$ (SC-XRD) MAPLE = 116 403 kJ mol^{-1}	$\frac{1}{2}Pr_2O_3$[61] + $1.5WO_3$[60] + $2.5Na_2WO_4$[11] MAPLE = 116 700 kJ mol^{-1} (Δ = 0.26%)
$Na_5Sm(WO_4)_4$ (SC-XRD) MAPLE = 116 571 kJ mol^{-1}	$\frac{1}{2}Sm_2O_3$[57] + $1.5WO_3$[60] + $2.5Na_2WO_4$[11] MAPLE = 116 905 kJ mol^{-1} (Δ = 0.29%)
$Na_5Eu(WO_4)_4$ (SC-XRD) MAPLE = 116 575 kJ mol^{-1}	$\frac{1}{2}Eu_2O_3$[57] + $1.5WO_3$[60] + $2.5Na_2WO_4$[11] MAPLE = 116 947 kJ mol^{-1} (Δ = 0.32%)
$Na_5Tb(WO_4)_4$ (SC-XRD) MAPLE = 116 917 kJ mol^{-1}	$\frac{1}{2}Tb_2O_3$[62] + $1.5WO_3$[60] + $2.5Na_2WO_4$[11] MAPLE = 117 038 kJ mol^{-1} (Δ = 0.10%)
$Na_5Ho(WO_4)_4$ (SC-XRD) MAPLE = 116 787 kJ mol^{-1}	$\frac{1}{2}Ho_2O_3$[63] + $1.5WO_3$[60] + $2.5Na_2WO_4$[11] MAPLE = 117 106 kJ mol^{-1} (Δ = 0.27%)
$Na_5Ho(WO_4)_4$ (Rietveld) MAPLE = 117 448 kJ mol^{-1}	$\frac{1}{2}Ho_2O_3$[63] + $1.5WO_3$[60] + $2.5Na_2WO_4$[11] MAPLE = 117 106 kJ mol^{-1} (Δ = 0.29%)
$Na_5Yb(WO_4)_4$ (SC-XRD) MAPLE = 116 917 kJ mol^{-1}	$\frac{1}{2}Yb_2O_3$[64] + $1.5WO_3$[60] + $2.5Na_2WO_4$[11] MAPLE = 117 167 kJ mol^{-1} (Δ = 0.29%)
$Na_5Bi(WO_4)_4$ (SC-XRD) MAPLE = 116 685 kJ mol^{-1}	$\frac{1}{2}Bi_2O_3$[65] + $1.5WO_3$[60] + $2.5Na_2WO_4$[11] MAPLE = 116 681 kJ mol^{-1} (Δ = 0.00%)

chemically comparable rare earth oxides, sodium tungstate and tungsten trioxide (Table 2). The deviations are well below 1% for all structures, which is our empirical benchmark for electrostatic consistency. The same holds true for $NaEu(WO_4)_2$. Here, the calculation was performed in the subgroup $I\bar{4}$ resolving the disorder of Na^+ and Eu^{3+}. Moreover, all coordination numbers were confirmed by our calculations.

Crystallographic relationships

$NaM(WO_4)_2$ and $Na_5M(WO_4)_4$ are two closely related structures with the former being the decomposition product of the latter and both crystallising in the same space group $I4_1/a$. For the sake of clarity and better understanding of this affinity, the systematic crystallographic relationship of $Na_5M(WO_4)_4$ to $NaM(WO_4)_2$ shown exemplarily on $Na_5Eu(WO_4)_4$ and $NaEu(WO_4)_2$ can be illustrated best by a group–subgroup relation scheme following the Bärnighausen formalism (Fig. S10†).[48,49] The volume ratio suggests that $Na_5Eu(WO_4)_4$ essentially represents a five-fold superstructure of *scheelite* type $NaEu(WO_4)_2$. The lower symmetric $Na_5Eu(WO_4)_4$ can be derived by a symmetry reduction of $NaEu(WO_4)_2$ to the isomorphic subgroup $I4_1/a$ according to the transformation $\mathbf{a} + 2\mathbf{b}, -2\mathbf{a} + \mathbf{b}, \mathbf{c}$ – isomorphic transitions of index 5 (i5) are rare and have been reviewed recently.[66] Hence, the special Wyckoff positions 4*a* and 4*b* split into 4*a* and 16*f* and 4*b* and 16*f*, respectively. The W^{6+} ion no longer occupies a special position, whereas Eu^{3+} is located on the 4*a* position and Na^+ occupies both the special position 4*b* and the general position 16*f*. The Na^+ at 4*b* is tetrahedrally coordinated since its position is derived from tetrahedrally coordinated W^{6+}. The other Na^+ is coordinated by six oxygen atoms with the polyhedron derived from the dodecahedron of $NaEu(WO_4)_2$ *via* the removal of two corners and the subsequent rearrangement of the oxygen atoms. The oxygen position itself splits as well leaving one of the five new positions vacant as expected since 20 Na, 4 Eu, 16 W and 64 O atoms were put onto 20 Na/Eu, 20 W and 80 O positions of the scheelite structure and there is less charge to be compensated by the oxygen anions. One oxygen atom is fourfold coordinated while the other three remain with a coordination number of 3.

Visually, the derivation of $Na_5Eu(WO_4)_4$ from $NaEu(WO_4)_2$ can be illustrated by the respective cation substructure shown in Fig. 6.[5,46] Besides local distortion, the cations are distributed in the same way in both structures forming layers perpendicular to the *c* axis containing two types of series (see also Fig. 2 and 3). $Na_5Eu(WO_4)_4$ is derived from $NaEu(WO_4)_2$ by replacing one fifth of the W^{6+} ions by Na^+ ions resulting in one NaO_4 alternating with four WO_4 along the tetrahedra series. Moreover, the disorder of Na^+ and Eu^{3+} vanishes and the former series of Na/Eu is replaced by alternations of four Na^+ and one Eu^{3+} ions. This results in minor changes in the cation positions already shown in Fig. 3 and major changes in the anion substructure, even leading to one herein vacant oxygen position. This oxygen atom is now found in the second coordination sphere of the W^{6+} ions. While tungsten is surrounded by an oxygen tetrahedron in the first coordination sphere for both $NaEu(WO_4)_2$ and $Na_5Eu(WO_4)_4$ the tetrahedron is tetracapped in the second coordination sphere in the former and tricapped in the latter (see Fig. S11†). One should note that the Eu^{3+} ions occupy a position coordinated by four $WO_4{}^{2-}$ anions.

Furthermore, the crystal structure can elucidate the thermal behavior of $Na_5Eu(WO_4)_4$. In the light of the decomposition of $Na_5Eu(WO_4)_4$ to $NaEu(WO_4)_2$ and Na_2WO_4, domains of both decomposition products may be found within the unit cell of $Na_5Eu(WO_4)_4$ (Fig. 7). Consequently, one unit cell formally contains two parts of $NaEu(WO_4)_2$ (red rectangles) and four

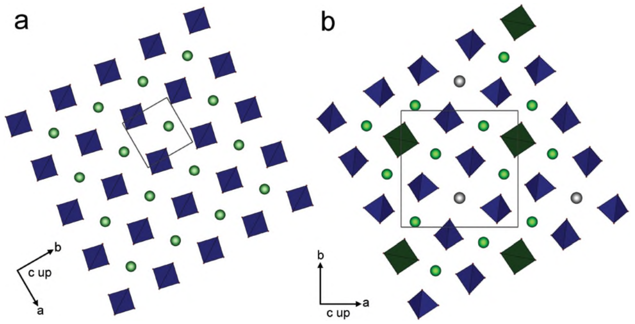

Fig. 6 Cation layer perpendicular to [001] in (a) $NaEu(WO_4)_2$ and (b) $Na_5Eu(WO_4)_4$: the unit cells are shown with a rotation of *circa* 60° in (a); blue tetrahedra represent WO_4 and dark green ones NaO_4, and the white spheres are shown for Eu^{3+}, green ones for Na^+ and pale green ones for disordered Na^+/Eu^{3+}.

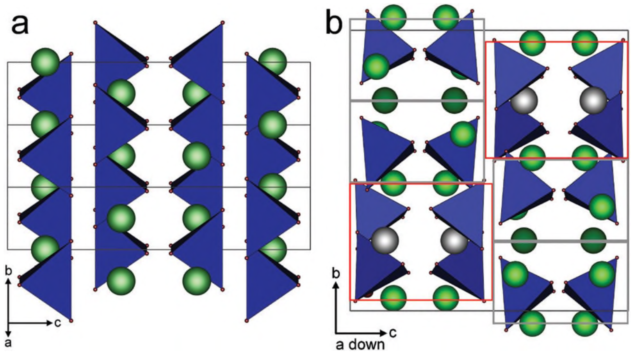

Fig. 7 Domain structure in the unit cell of $Na_5Eu(WO_4)_4$ (b) with $NaEu(WO_4)_2$ (red rectangles) and Na_2WO_4 (grey rectangles) resembling regions; (a) shows the unit cell of $NaEu(WO_4)_2$ rotated around the *c* axis for 63.4°: this view shows the similarity of the $NaEu(WO_4)_2$ unit cell (a) and the $NaEu(WO_4)_2$ related domain in $Na_5Eu(WO_4)_4$ (red rectangle in (b)).

parts of Na_2WO_4 (grey rectangles) representing the stoichiometry of the decomposition products – such a behaviour is also known as chemical twinning. While the domains of $NaEu(WO_4)_2$ include Na^+ and Eu^{3+} on the defined positions, disorder is introduced in the independent $NaEu(WO_4)_2$ during crystallisation. The concept of such chemical twinning is also known from phosphate tungstate compounds.[3] In conclusion, the thermal decomposition of $Na_5Eu(WO_4)_4$ appears to be predetermined within its crystal structure.

Thermal decomposition of $Na_5M(WO_4)_4$

The thermal decomposition of $Na_5M(WO_4)_4$ according to the reaction equation

$$Na_5M(WO_4)_4 \rightarrow NaM(WO_4)_2 + 2Na_2WO_4$$

accompanied by simultaneous melting was investigated by differential scanning calorimetry (DSC). The results in Fig. S12† show one endothermic peak for all measurements on $Na_5M(WO_4)_4$ (M = La, Pr, Eu, Gd, Tb, Ho, Yb, Lu, Bi). The maxima of the peaks were taken as decomposition temperatures T_D. Fig. 8 shows the decomposition temperature against the ionic radii of the respective rare earth ions M^{3+}.[51] For M = La, Eu, Lu and Bi, the values are in accordance with earlier reports.[5,35,43,44] There is a maximum in T_D around 754 °C for $Na_5Ho(WO_4)_4$. Thus, T_D does not follow linearly the lanthanide contraction. Rather, the behaviour of T_D can be correlated to the difference of the ionic radii of M^{3+} and Na^+ in $Na_5M(WO_4)_4$ with CN = 8 and CN = 6, respectively. According to the earlier discussion of the crystal structure and the existence of domains, M^{3+} and Na^+ get disordered during the formation of $NaM(WO_4)_2$ due to thermodynamic reasons.[15] The energy benefit of this process scales with the difference of the ionic radii $|r(M) - r(Na)|$ in $Na_5M(WO_4)_4$. Consequently, the maximal external energy in the form of temperature is necessary for decomposition in the case of $Na_5Ho(WO_4)_4$ due to the minimal difference in the ionic radii (Fig. 8). $Na_5Bi(WO_4)_4$ is decomposed while melting at 640 °C. The large difference cannot be explained by the ionic radii. It is presumably due to the lack of f electrons in Bi^{3+}.

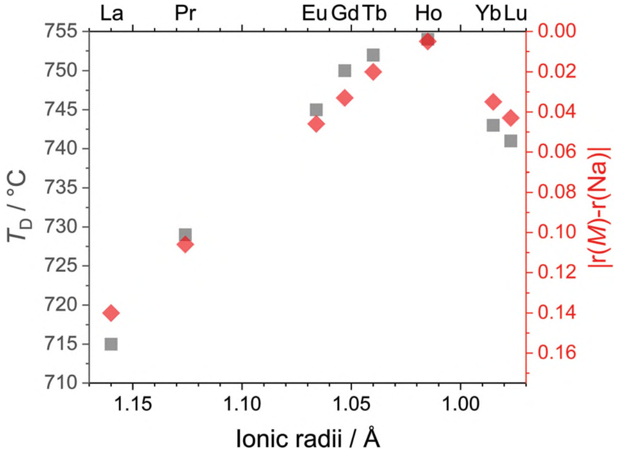

Fig. 8 Behaviour of the thermal decomposition temperature T_D of $Na_5M(WO_4)_4$ (grey) with the ionic radii of M^{3+} correlated to the difference of the ionic radii of M^{3+} with CN = 8 and Na^+ with CN = 6 (red).[51]

Miscibility gap in $Na_5Y_{1-x}Eu_x(WO_4)_4$ and $Na_5Y_{1-y}Tb_y(WO_4)_4$

In contrast to earlier works,[6,31,33,34,43] we could demonstrate the existence of a temperature dependent miscibility gap in both $Na_5Y_{1-x}Eu_x(WO_4)_4$ and $Na_5Y_{1-y}Tb_y(WO_4)_4$. Samples of the compositions $Na_5Y_{0.5}Eu_{0.5}(WO_4)_4$ and $Na_5Y_{0.5}Tb_{0.5}(WO_4)_4$ were prepared *via* flux syntheses at 600 °C. Rietveld refinements displayed in Fig. S13 and S14† showed the presence of two separated phases in $Na_5Y_{0.5}Eu_{0.5}(WO_4)_4$ and $Na_5Y_{0.5}Tb_{0.5}(WO_4)_4$, *i.e.* $Na_5Y(WO_4)_4$ *vs.* $Na_5Eu(WO_4)_4$ and $Na_5Tb(WO_4)_4$ *vs.* $Na_5Y(WO_4)_4$. The details are presented in Table S10.† Single crystals were grown from the melt at 800 °C for both samples. The single-crystal X-ray structure determinations yielded single-phased $Na_5Y_{0.49}Eu_{0.51}(WO_4)_4$ and $Na_5Y_{0.49}Tb_{0.51}(WO_4)_4$. The details can be found in Table S11.† Consequently, the miscibility gap could be closed *via* melting the compounds at 800 °C. This was confirmed by Rietveld refinements (Table S12, Fig. S14 and S15†) showing the three phases $Na_5Y_{0.5}Eu_{0.5}(WO_4)_4$, $NaY_{0.5}Eu_{0.5}(WO_4)_2$ plus Na_2WO_4 and $Na_5Y_{0.5}Tb_{0.5}(WO_4)_4$, $NaY_{0.5}Tb_{0.5}(WO_4)_2$ plus Na_2WO_4, respectively. Both sets of lattice parameters for $Na_5Y_{0.49}Eu_{0.51}(WO_4)_4$ determined by single-crystal XRD and Rietveld refinement agree with Vegard's law[67] yielding a mean Eu^{3+} content of 51.9 ± 1.4% close to the result from single crystal XRD of 51.2 ± 0.3%. For $Na_5Y_{0.49}Tb_{0.51}(WO_4)_4$, the Tb^{3+} content derived from the lattice parameters determined from Rietveld refinement according to Vegard's law[67] is 50 ± 3% being close to the content from single crystal XRD of 51.4 ± 0.2%. However, the lattice parameters of $Na_5Y_{0.49}Tb_{0.51}(WO_4)_4$ from single-crystal data do not follow Vegard's law.

Additionally, two samples of the stoichiometry $Na_5Y_{0.5}Eu_{0.5}(WO_4)_4$ were synthesised *via* solid state reactions A1 and A2 reported in the literature at 600 °C and 700 °C, respectively. According to Rietveld refinements of the respective powder XRD pattern (Table S10 and Fig. S16†), synthesis A1 yielded a two-phased product, while a single phase of $Na_5Y_{0.5}Eu_{0.5}(WO_4)_4$ was obtained by synthesis A2. In both cases, there is a considerable side phase of $NaY_{0.5}Eu_{0.5}(WO_4)_2$. It is worth noting that the side phase after synthesis A1 is comprised of two separated phases $NaY(WO_4)_2$ and $NaEu(WO_4)_2$, too. Consequently, the miscibility gap in $Na_5Y_{1-x}Eu_x(WO_4)_4$ is temperature-dependent since it is not related to the type of synthesis. The energy available during the synthesis at 600 °C is sufficient to form $Na_5M(WO_4)_4$ but not for the M^{3+} ions to interchange. At 700 °C synthesis temperature, there is no miscibility gap. Using variable temperature XRD, the gap could be narrowed to 660 °C–700 °C (see Fig. S17†). This temperature provides sufficient activation energy for the M^{3+} ions' interchange. The investigation of the 'width' of the miscibility gap in the concentration is difficult due to the proximity of the reflections of $Na_5Y(WO_4)_4$ and $Na_5Eu(WO_4)_4$. The splitting of the dominant (321), (312) and (213) reflections around 2θ = 29.5° was only unambiguously observed for $x = 0.5$ but not for $x = 0.1$.

Optical properties of $Na_5M(WO_4)_4$

The infrared spectra of $Na_5M(WO_4)_4$ (Fig. S18†) show five distinct absorption bands of the $WO_4{}^{2-}$ group. The symmetric stretching of $WO_4{}^{2-}$ appears at 935 cm^{-1} and the antisymmetric stretching at 893 cm^{-1}, 847 cm^{-1}, 824 cm^{-1} and 752–766 cm^{-1}.[35,45] In accordance with the results of the structure determination, there are no changes in the position of these bands since the W–O distances do not differ with the lanthanide contraction (Tables S6–S9†). Furthermore, around 400 cm^{-1}, the M–O vibration appears[68] moving to higher wavenumbers with the decrease of the M–O distance following the lanthanide contraction (Tables S6–S9†).

The UV/Vis spectra of $Na_5M(WO_4)_4$ presented in Fig. S19† show all the expected f–f transitions for the rare earth ions Pr^{3+}, Nd^{3+}, Sm^{3+}, Eu^{3+}, Dy^{3+}, Ho^{3+}, Er^{3+}, and Tm^{3+}, the 4f–5d transition of Ce^{3+} and the s–p transition of Bi^{3+} along with the broad absorption around 230 nm due to the O^{2-}–W^{6+} ligand to metal charge transfer (LMCT).[3,9,33,34,43,69–72] These transitions will be discussed in detail along with the results of fluorescence spectroscopy in the following. A detailed assignment of the absorption bands in the UV/Vis spectra is presented in Table S12.† $Na_5Ho(WO_4)_4$ shows a pronounced Alexandrite effect also known from other Ho^{3+} compounds,[23,73,74] *i.e.* it appears pink under light emission of luminescent tubes and yellow-beige under ambient day light due to the different spectral compositions of both light sources.

The fluorescence spectra of $Na_5M(WO_4)_4$ (M = Pr, Sm, Eu, Tb, Tm) show the characteristic excitation and emission of the f–f transitions. For the sake of better readability and clarity we omit most of the wavelength values which can be found in Table S13.† The emission can be excited both directly at the M^{3+} ion and using the O^{2-}–W^{6+} LMCT as an antenna.[3,36,40,41] In general, an energy transfer from the O^{2-}–W^{6+} LMCT antenna towards the M^{3+} ion is possible *via* three different mechanisms. The first option is the Dexter mechanism relying on exchange interactions consequently requiring covalence between sensitiser and activator.[75] This mechanism is expected to be of little importance in $Na_5M(WO_4)_4$ due to the compounds' ionic nature (Tables S6–S9†). Secondly, the Förster mechanism assumes energy transfer *via* electric dipole transitions governed by the distance between sensitiser and activator.[76,77] In principle, this type of energy transfer is likely to occur in $Na_5M(WO_4)_4$ in the light of the distances discussed earlier being smaller than the critical transfer distance.[36] The third possibility is the excitation of the activator *via* the luminescence emission of the sensitiser.[4] For $Na_5Gd(WO_4)_4$ having no relevant f–f transitions in the regime under discussion, a broad W^{6+}–O^{2-} LMCT emission centred at 470 nm is reported at 20 K (ref. 36) while a broad emission around 460 nm could be observed for the $Na_5Y(WO_4)_4$ sample at 77 K (Fig. S20†).

$Na_5Pr(WO_4)_4$. $Na_5Pr(WO_4)_4$ exhibits the characteristic deep red emission of Pr^{3+} ($^3P_0 \rightarrow {}^3H_2$) accompanied by greenish-blue emission ($^3P_0 \rightarrow {}^3H_4$) for both excitation wavelengths shown in Fig. 9.[12] This can be explained by the ability of the W^{6+}–O^{2-} LMCT emission to excite Pr^{3+}.[4,36,42] Consequently, an effective energy transfer from the $WO_4{}^{2-}$ group to the Pr^{3+} ion is possible. The excitation spectrum shows on the one hand the intensity of the LMCT excitation obviously being higher compared to excitation *via* the parity forbidden f–f transitions and on the other hand the manifestation of the energy transfer from the $WO_4{}^{2-}$ group to Pr^{3+} in general. These properties are expected for all $Na_5M(WO_4)_4$ samples studied for their fluorescent properties. Moreover, Pr^{3+}doped titanates, orthovanadates and niobates show low-lying intervalence charge transfer (IVCT) states resulting in a fast multi-phonon non-radiative relaxation process from ($^3P_0 \rightarrow {}^1D_2$) and consequently leading to a main emission around 600 nm ($^1D_2 \rightarrow {}^3H_4$). In distinct dissimilarity, tungstates show weak emission from the $^1D_2$ state only.[12,78–80] For $Na_5Pr(WO_4)_4$, only a very weak emission due to the $^1D_2 \rightarrow {}^3H_4$ transition was measured. The IVCT state in tungstates is located at higher energies.[79,80] The relaxations from $^3P_0$ to $^1D_2$ were correlated with both the Pr–W and Pr–O distances taking into account both the first and second coordi-

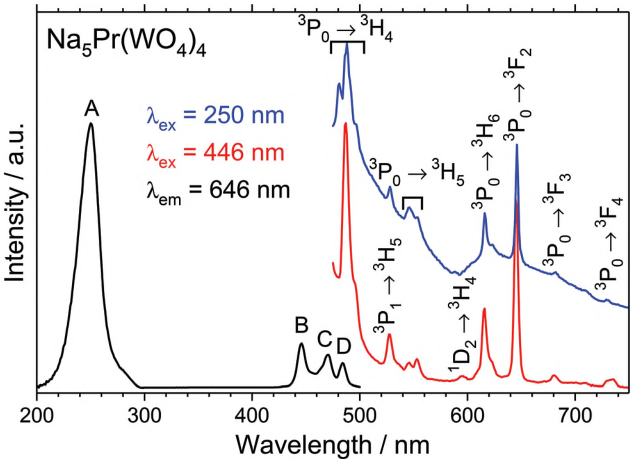

Fig. 9 Excitation and emission spectra of $Na_5Pr(WO_4)_4$: the assignment of the peaks can be found in Table S13;† the excitation spectra were corrected with respect to the lamp intensity.

nation environments of the Pr^{3+} ions.[79] The large distances determined from the single crystal data of Pr–W around 3.86 Å and Pr–O around 2.46 Å are – in accordance with the data reported in the literature[79] – responsible for only weak non-radiative relaxation ($^3P_0 \rightarrow {}^1D_2$). Consequently, the emission of $Na_5Pr(WO_4)_4$ is dominated by transitions originating at the $^3P_0$ state at both excitation *via* the O^{2-}–W^{6+} LMCT antenna and the Pr^{3+} f–f transitions. The Pr^{3+} $4f^2 \rightarrow 4f^15d^1$ band is expected to be located at higher energies than the measured range due to the large Pr–O distances.[80]

$Na_5Sm(WO_4)_4$. The fluorescence emission spectra shown in Fig. 10 of the red phosphor $Na_5Sm(WO_4)_4$ provide further information on the symmetry of the Sm^{3+} ions' position. Excited using either the Sm^{3+} f–f transitions or the O^{2-}–W^{6+} LMCT two major emission peaks were observed $\left(4G_{\frac{5}{2}} \rightarrow {}^6H_{\frac{7}{2}} \text{ and } {}^4G_{\frac{5}{2}} \rightarrow {}^6H_{\frac{9}{2}}\right)$. The three major transitions of Sm^{3+} are $^4G_{\frac{5}{2}} \rightarrow {}^6H_{\frac{5}{2}}$, $^6H_{\frac{7}{2}}$ and $^6H_{\frac{9}{2}}$. The first is dominated by the magnetic dipole transition and the third by electronic dipole transition, while $^4G_{\frac{5}{2}} \rightarrow {}^6H_{\frac{7}{2}}$ is partly of both magnetic and electric dipole nature. In accordance with the determined crystal structure, the highest intensity was observed for the $^4G_{\frac{5}{2}} \rightarrow {}^6H_{\frac{9}{2}}$ transition since the Sm^{3+} ion is located on a lattice site without inversion symmetry resulting in the hypersensibilisation of the electronic dipole transition $^4G_{\frac{5}{2}} \rightarrow {}^6H_{\frac{9}{2}}$.[14,81] Furthermore, the red emission is observed despite the Sm^{3+} ions' ability to perform Sm^{3+}–Sm^{3+} ion pair cross-relaxation because of equidistant pairs of energy levels resulting in emission quenching at low concentrations of Sm^{3+}.[14,70,81] This is in accordance with the large Sm^{3+}–Sm^{3+} distances resulting in the special property of $Na_5M(WO_4)_4$ to show no concentration quenching as discussed in the crystal structure section (Fig. 5).[26,30,32,33,35]

$Na_5Eu(WO_4)_4$. In the excitation spectrum of $Na_5Eu(WO_4)_4$, the broad peaks of the O^{2-}–W^{6+} LMCT and the O^{2-}–Eu^{3+} LMCT overlap.[17,82–85] Again, excitation using both the f–f transitions of Eu^{3+} and the LMCT is possible leading to the characteristic orange-red Eu^{3+} emission.[36,72,81,83] Due to the high site symmetry of Eu^{3+} the $^5D_0 \rightarrow {}^7F_1$ transition does not split and is thus in accordance with the determined crystal structure of $Na_5Eu(WO_4)_4$.[50,83] The hypersensitivity of the $^5D_0 \rightarrow {}^7F_2$ transition is in agreement with earlier reports on $Na_5Eu(WO_4)_4$ and $Na_5Eu(MoO_4)_4$ and the lack of inversion symmetry at the Eu^{3+} ions' lattice site.[30,32,34,43,50,83]

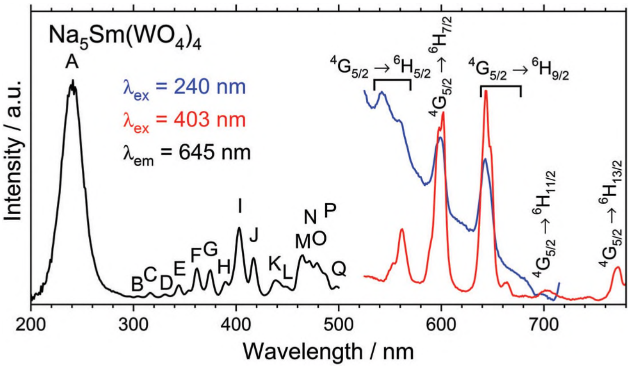

Fig. 10 Excitation and emission spectra of $Na_5Sm(WO_4)_4$: the assignment of the peaks can be found in Table S13;† the excitation spectra were corrected with respect to the lamp intensity.

$Na_5Y_{1-x}Eu_x(WO_4)_4$. The fluorescence spectra of the solid solution $Na_5Y_{1-x}Eu_x(WO_4)_4$ resemble the spectra of $Na_5Eu(WO_4)_4$ (Fig. 11 and 12 and Table S13†). The expected shift of the O^{2-}–Eu^{3+} LMCT bands with the decreased Eu–O distance with lower values of x towards higher energies in the excitation spectra[83–85] could be observed. Both O^{2-}–Eu^{3+} and O^{2-}–W^{6+} LMCT bands overlap. Hence, the relative intensity of the LMCT band to the f–f transitions in the excitation spectra increases with decreasing Eu^{3+} content since the overlap of both bands is increasing. This is exemplarily shown for $Na_5Eu(WO_4)_4$ and $Na_5Y_{0.95}Eu_{0.05}(WO_4)_4$ using a Gaussian fit in Fig. S21.† While the O^{2-}–W^{6+} LMCT band is located at 239 nm

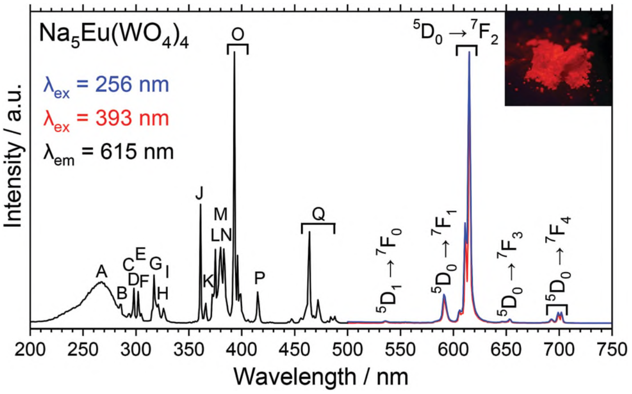

Fig. 11 Excitation and emission spectra of $Na_5Eu(WO_4)_4$: the assignment of the peaks can be found in Table S13;† the excitation spectra were corrected with respect to the lamp intensity; the inset shows a picture of $Na_5Eu(WO_4)_4$ powder under 254 nm UV radiation.

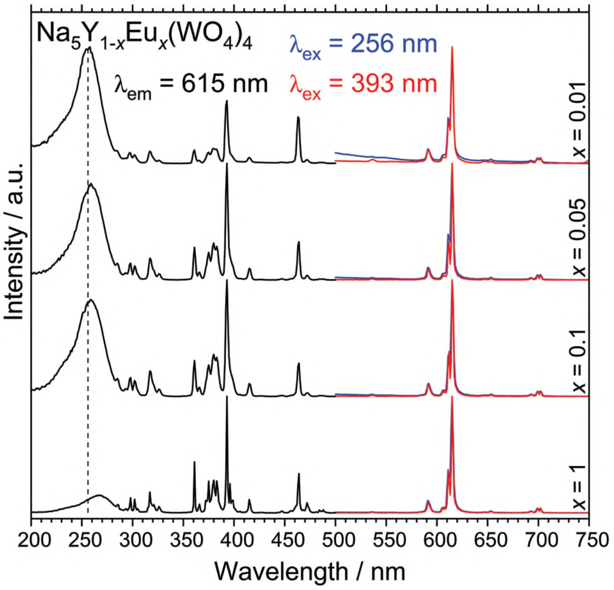

Fig. 12 Excitation and emission spectra of $Na_5Y_{1-x}Eu_x(WO_4)_4$ (x = 0.01, 0.05, 0.1, 1): the assignment of the peaks of $Na_5Eu(WO_4)_4$ (x = 1) can be found in Table S13.† There are no additional peaks for the three other samples. However, there is an increase in the intensity ratio of the broad LMCT band around 260 nm and the f–f transition excitation with its maximum at 393 nm ($^7F_0 \rightarrow {}^5L_6$) with decreasing x accompanied by a shift of the O^{2-}–Eu^{3+} LMCT band to lower wavelengths with decreasing x elucidated by the dotted line in the graph at 256 nm. The excitation spectra were corrected with respect to the lamp intensity.

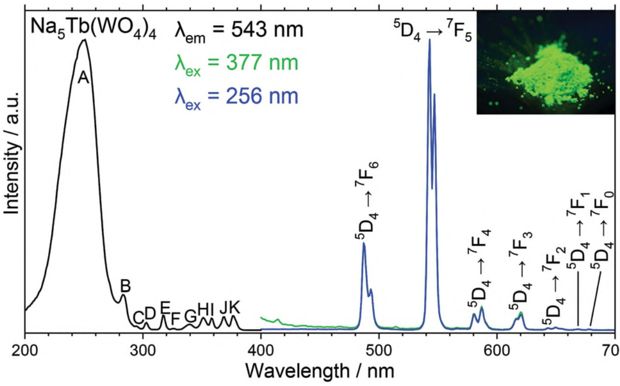

Fig. 13 Excitation and emission spectra of $Na_5Tb(WO_4)_4$: the assignment of the peaks can be found in Table S13;† the excitation spectra were corrected with respect to the lamp intensity; the inset shows a picture of $Na_5Tb(WO_4)_4$ powder under 254 nm UV radiation.

for both compounds, there is a shift of the O^{2-}–Eu^{3+} LMCT band from 266.5 nm in $Na_5Eu(WO_4)_4$ to 260.5 nm in $Na_5Y_{0.95}Eu_{0.05}(WO_4)_4$. The former value is almost identical to the one recently reported for $Eu_2[B_2(SO_4)_6]$[19] indicating a weak coordination of Eu^{3+} in $Na_5Eu(WO_4)_4$. Both values are in the typical region for oxide coordinated europium compounds.[82]

In contrast to the ambiguous powder XRD pattern of $Na_5Y_{0.9}Eu_{0.1}(WO_4)_4$ discussed earlier, the clear difference between the spectra of $Na_5Y_{0.9}Eu_{0.1}(WO_4)_4$ and $Na_5Eu(WO_4)_4$ indicates that $Na_5Y_{0.9}Eu_{0.1}(WO_4)_4$ is an actual solid solution and not a phase mixture of $Na_5Y(WO_4)_4$ and $Na_5Eu(WO_4)_4$ providing further insight into the width of the miscibility gap in $Na_5Y_{1-x}Eu_x(WO_4)_4$.

$Na_5Tb(WO_4)_4$. $Na_5Tb(WO_4)_4$ emits green light due to the characteristic $^5D_4 \rightarrow {}^7F_J$ transitions of Tb^{3+} upon both excitation *via* the O^{2-}–W^{6+} LMCT, which overlays the Tb^{3+} f–d transitions, and the Tb^{3+} f–f transitions (Fig. 13). The absence of a broad emission band between 450 nm and 500 nm due to the W^{6+}–O^{2-} LMCT emission while excited at the O^{2-}–W^{6+} LMCT indicates an effective energy transfer towards the Tb^{3+} ion.[36] As expected, there is no blue emission in $Na_5Tb(WO_4)_4$ due to Tb^{3+}–Tb^{3+} cross-relaxation.[33,69] This effect will be discussed in detail along with the $Na_5Y_{1-y}Tb_y(WO_4)_4$ samples later. The excitation spectrum of $Na_5Tb(WO_4)_4$ shows a very high LMCT band, especially compared to the excitation spectrum of $Na_5Eu(WO_4)_4$. The intensity of the LMCT band is similar for $Na_5Pr(WO_4)_4$ and $Na_5Sm(WO_4)_4$. These findings are in accordance with the literature on double tungstates[9,17] and can be explained by the better matching of the LMCT emission with the Pr^{3+}, Sm^{3+} and Tb^{3+} excitation spectra than with the Eu^{3+} excitation bands. There is only the $^7F_0 \rightarrow {}^5D_2$ transition accessible by the LMCT emission centred at 470 nm, while multiple f–f transitions can be excited in $Na_5Pr(WO_4)_4$ (Fig. 9) and $Na_5Sm(WO_4)_4$ (Fig. 10) and in $Na_5Tb(WO_4)_4$ (Fig. 13) the $^7F_6 \rightarrow {}^5D_4$ transition can be excited effectively.

$Na_5Y_{1-y}Tb_y(WO_4)_4$. Compared to $Na_5Tb(WO_4)_4$, the $Na_5Y_{1-y}Tb_y(WO_4)_4$ samples show an additional blue emission originating in the $^5D_3$ state increasing in intensity with lower Tb^{3+} content when excited at 377 nm (Fig. 14). This can be

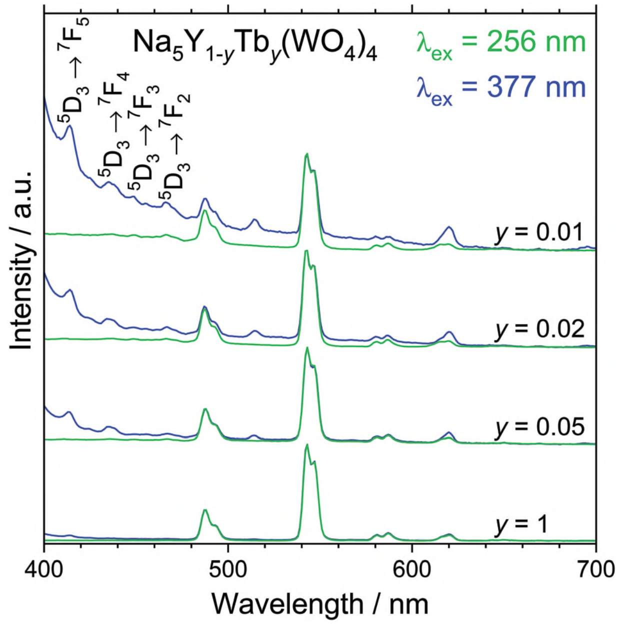

Fig. 14 Emission spectra of $Na_5Y_{1-y}Tb_y(WO_4)_4$ (y = 0.01, 0.02, 0.05, 1): the assignment of the peaks of $Na_5Tb(WO_4)_4$ (y = 1) can be found in Table S13;† there is an additional blue emission originating in the $^5D_3$ state of Tb^{3+} for low values for y; the respective transitions are indicated inside the graph.

explained by the less effective cross relaxation process between an excited Tb^{3+} ion and an adjacent ground state Tb^{3+} ion $^5D_3(Tb^{3+}) + {}^7F_6(Tb^{3+}) \rightarrow {}^5D_4(Tb^{3+}) + {}^7F_0(Tb^{3+})$ in low doped $Na_5Y_{1-y}Tb_y(WO_4)_4$ samples. The cross relaxation depends on the distance of neighboring Tb^{3+} ions and is consequently minimised at low doping concentration.[33,69] Hence, the ratio of the Tb^{3+} emissions originating in the $^5D_3$ state to the ones from the $^5D_4$ state decreases with the Tb^{3+} content (see Fig. S22†). The presence of the blue Tb^{3+} emissions originating in the $^5D_3$ state up to doping concentrations of 5% in $Na_5Y_{1-y}Tb_y(WO_4)_4$ confirms a rather weak coordination of Tb^{3+}.[19,69] For comparison, no emission from the $^5D_3$ state was observed in $NaGd(WO_4)_2$:Tb^{3+} down to doping concentrations of 1%.[8] This is presumably due to the considerably smaller average M–M distances in $NaM(WO_4)_2$ compared to $Na_5M(WO_4)_4$ (Tables S5–S9†).

Furthermore, the blue emission is absent when the phosphor is excited *via* the LMCT for all doping concentrations. The broad LMCT emission is able to excite Tb^{3+} to the $^5D_4$ state, only. The transferred energy is not sufficient to reach the $^5D_3$ state.[4,42,86] The respective energy levels are sketched in Fig. S23.† Consequently, the blue emission originating from the latter is not present. The excitation spectra of $Na_5Y_{1-y}Tb_y(WO_4)_4$ (Fig. S24†) resemble that of $Na_5Tb(WO_4)_4$, but they show a slight decrease of the ratio of LMCT to f–f transitions with increasing Tb^{3+} content presumably resulting from the different overlap of the O^{2-}–W^{6+} LMCT and the Tb^{3+} f → d transitions due to the smaller Tb–O distances at lower doping concentrations (see Tables S7 and S9†).

Consequently, the absence of the blue emission when exciting at the $WO_4{}^{2-}$ antenna can be elucidated by an energy transfer from $WO_4{}^{2-}$ to Tb^{3+} *via* the luminescence emission of the W^{6+}–O^{2-} LMCT.[4] An energy transfer based on an electric dipole–dipole interaction as reported earlier[36] for the phosphor class appears to be merely of minor significance. In this case, the blue Tb^{3+} emission would not be absent when exciting at the $WO_4{}^{2-}$ antenna.

$Na_5Tm(WO_4)_4$. $Na_5Tm(WO_4)_4$ shows a sharp blue emitting line ($^1D_2 \rightarrow {}^3F_4$) (Fig. 15). The emission can be excited primarily by the $^3D_6 \rightarrow {}^1D_2$ transition accompanied by the two weak transitions $^3H_6 \rightarrow {}^3P_2$ and $^3H_6 \rightarrow {}^1I_6$. Distinctly different from all other studied compounds there was no O^{2-}–W^{6+} LMCT excitation observed in $Na_5Tm(WO_4)_4$. This is in agreement with the earlier results for $NaGd(WO_4)_2$:Tm^{3+}.[10,13] Apparently, there is no energy transfer from the $WO_4{}^{2-}$ antenna towards the Tm^{3+} ion. Both O^{2-}–W^{6+} LMCT excitation and W^{6+}–O^{2-} LMCT emission cannot be seen in Fig. 15 since they are much weaker than the Tm^{3+} f–f transitions in the same regions of the spectrum.

Presumably, the energy transfer cannot take place due to the overlap of the emissions of Tm^{3+} ($^1D_2 \rightarrow {}^3F_4$) and the W^{6+}–O^{2-} LMCT. The energy transferred from the LMCT is not sufficient for Tm^{3+} to reach the $^1D_2$ state. In contrast, an energy transfer from the O^{2-}–W^{6+} LMCT to Tm^{3+} is reported in $CaWO_4$:Tm^{3+} (ref. 7) since the W^{6+}–O^{2-} LMCT emission is located at higher energies compared to $Na_5Tm(WO_4)_4$.

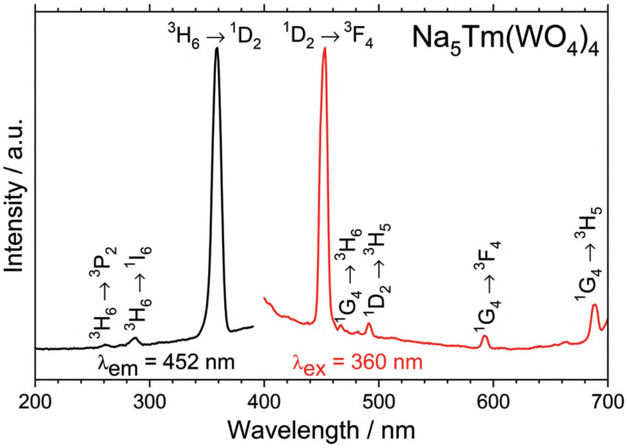

Fig. 15 Excitation and emission spectra of $Na_5Tm(WO_4)_4$: the assignment of the peaks can be found in Table S13;† the excitation spectra were corrected with respect to the lamp intensity.

$Na_5Bi(WO_4)_4$. The luminescence properties of $Na_5Bi(WO_4)_4$ were studied both at room temperature and at 77 K (Fig. 16). The compound shows a broad blue emission centred due to the $^3P_1 \rightarrow {}^1S_0$ transition of Bi^{3+} at both temperatures. Out of the $6s^2$ ground state of Bi^{3+} ($^1S_0$) and the excited 6s6p states ($^3P_0$, $^3P_1$, $^3P_2$ and $^1P_1$ in sequence of increasing energy) the $^1S_0 \rightarrow {}^1P_1$ transition is parity and spin-allowed and the $^1S_0 \rightarrow {}^3P_1$ transition is partially allowed thanks to spin–orbit coupling. The other transitions are strictly forbidden. However, they may appear due to mixing enabled by low local symmetry.[34,82] Consequently, the $^1S_0 \rightarrow {}^1P_1$ and $^1S_0 \rightarrow {}^3P_1$ transitions emerge in the excitation spectra superimposed with the O^{2-}–W^{6+} LMCT band. Three transitions could be assigned using Gaussian fits for both excitation spectra (Fig. S25†). At room temperature, we assigned the $^1S_0 \rightarrow {}^3P_1$ transition centred at 290 nm, the $^1S_0 \rightarrow {}^1P_1$ transition at 275 nm and the O^{2-}–W^{6+} LMCT at 258 nm, while the bands occur at 281 nm, 273 nm and 250 nm at 77 K, respectively. Both the LMCT and the $^1S_0 \rightarrow {}^3P_1$ transition are shifted to smaller wavelengths at

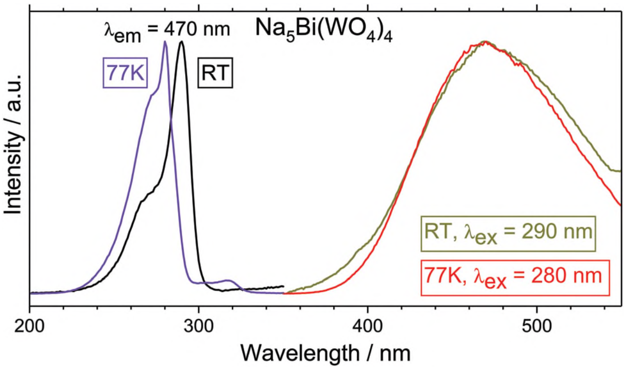

Fig. 16 Excitation and emission spectra of $Na_5Bi(WO_4)_4$ at both room temperature and 77 K: the assignment of the peaks can be found in Table S13;† please note that the excitation spectra are not corrected with respect to the lamp intensity.

77 K since more energy is necessary to surpass the respective threshold because of temperature-driven occupation of vibrational substrates. The spin-allowed $^1S_0 \rightarrow {}^1P_1$ transition is not significantly affected by temperature. The absence of other transitions is in agreement with the structure determination resulting in the 4*a* Wyckoff site for Bi^{3+} with site symmetry $\bar{4}$. Furthermore, the shift of the $^1S_0 \rightarrow {}^3P_1$ transition with temperature supports the conclusion of two different Bi^{3+} transitions instead of one transition with a doublet. The latter would require two independent Bi^{3+} sites.[16] According to our single-crystal XRD experiment, there is only one Bi^{3+} position in $Na_5Bi(WO_4)_4$. Since we fitted the non-corrected excitation spectra, the intensity of the LMCT is underestimated in the results.

Conclusion of the luminescence properties

In conclusion, the discussed fluorescence emission and excitation spectra confirm that there is no apparent concentration quenching in $Na_5M(WO_4)_4$ in agreement with the large M–M distances (Fig. 5). Moreover, all results indicate that the energy transfer from the sensitiser WO_4^{2-} to the activator M^{3+} is governed by the luminescence emission of the W^{6+}–O^{2-} LMCT.[4] In particular, the absence of blue emission in $Na_5Y_{1-y}Tb_y(WO_4)_4$ when excited *via* the O^{2-}–W^{6+} LMCT is not comprehensible by the other two mechanisms discussed earlier.[36,75–77]

Magnetic properties of $Na_5M(WO_4)_4$

For $Na_5M(WO_4)_4$ (M = Ce, Pr, Sm, Eu, Tb, Tm, Yb, Bi), the temperature dependence of the magnetic susceptibility (χ) was measured at 10 kOe and is plotted along with their inverse susceptibility χ^{-1} in Fig. 17 and S26.† The extracted magnetic data are presented in Table 3. All samples with the exception of $Na_5Bi(WO_4)_4$ show paramagnetism over the whole investigated temperature range. No onset of any magnetic interactions has been observed from these measurements. This can be attributed to the large M–M distances in $Na_5M(WO_4)_4$ (see Fig. 5). The inverse susceptibility was fitted in the temperature range from 75–300 K using the modified Curie–Weiss law. The calculated effective magnetic moments are in line with the respective rare-earth cations in the trivalent oxidation state. For $Na_5Sm(WO_4)_4$ and $Na_5Eu(WO_4)_4$ the typical van Vleck paramagnetic behaviour of Sm^{3+} and Eu^{3+} was observed, which will be discussed later.[50,87–95] The inverse susceptibilities (χ^{-1} data) of $Na_5Ce(WO_4)_4$ and $Na_5Yb(WO_4)_4$ deviate from the linear behaviour due to crystal field effects.

In addition, low-field measurements (not shown) with an applied magnetic field of 100 Oe were exemplarily performed for $Na_5Pr(WO_4)_4$ in the zero-field- and field-cooled mode (ZFC/FC). No magnetic ordering was observed down to 2.5 K. The magnetisation isotherms recorded at 3, 10 and 50 K are shown in Fig. S26c.† As expected for a paramagnetic material without a magnetic phase transition, the curves are linear. The saturation magnetisation at 3 K and 80 kOe reaches μ_{sat} = 0.31(1)μ_B, which is significantly below the calculated value according to $g_J \times J$ of $\mu_{sat,calc}$ = 3.20μ_B.

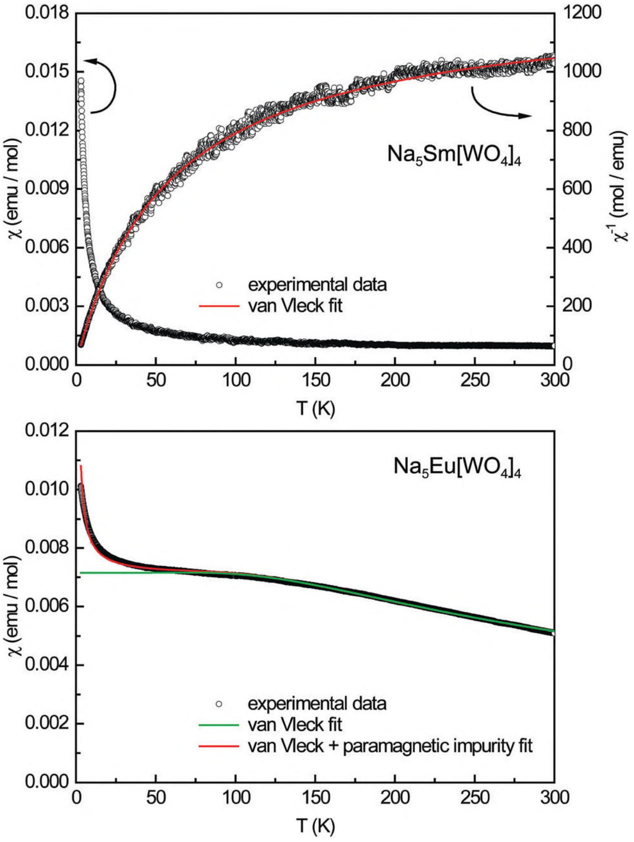

Fig. 17 Magnetic properties of $Na_5Sm(WO_4)_4$: (top) temperature dependence of the magnetic susceptibility (χ and χ^{-1} data) measured at 10 kOe along with the fit of the data (see the text); magnetic properties of $Na_5Eu(WO_4)_4$: (bottom) temperature dependence of the magnetic susceptibility (χ data) measured at 10 kOe along with the fit of the data (see the text).

Table 3 Magnetic properties of $Na_5M(WO_4)_4$ (M = Ce, Pr, Sm, Eu, Tb, Tm, Yb, Bi): μ_{eff}, effective magnetic moment; μ_{calc}, calculated magnetic moment; Θ_p, paramagnetic Curie temperature; the respective standard deviations are given in parentheses

M	μ_{eff}/μ_B	μ_{calc}/μ_B	Θ_p/K
Ce	2.38(1)	2.54	−103.6(1)
Pr	3.78(1)	3.62	−39.0(1)
Sm	0.61(1)	0.845	−0.3(1)
Eu	van Vleck, λ = 612(10) K, χ_0 = 5.6(1) × 10^{-3} emu mol^{-1}		
Gd	8.11(1)	7.94	+4.1(1)
Tb	9.77(1)	9.72	−0.8(1)
Tm	7.48(1)	7.56	−3.1(1)
Yb	4.71(1)	4.54	−43.6(1)
Bi	Diamagnetic; χ(300 K) = −190(1) × 10^{-6} emu mol^{-1}		

$Na_5Sm(WO_4)_4$ and $Na_5Eu(WO_4)_4$ exhibit the typical expected van Vleck type paramagnetism (Fig. 17). For the Sm^{3+} cations, it is caused by the close proximity of the excited J = 7/2 multiplet with respect to the ground state J = 5/2 multiplet. The energy difference between these states is only about 1550 K, while the respective other angular momentum levels are correspondingly higher. A very small paramagnetic moment of

$0.845\mu_B$ caused by an antiparallel coupling of the $L = 5$, $S = 5/2$ Russell–Saunders states is subsequently observed for free Sm^{3+} cations. In order to describe the magnetic behavior of samarium compounds, Stewart developed a theory with the unexpected simple form $\chi(T) = \chi_0 + D/(T - \Theta)$.[90] D was defined as the effective Curie constant by the authors. Hamaker and coworkers were able to prove that $\chi(T)$ for polycrystalline $SmRh_4B_4$ can be described by the equation

$$\chi_M(T) = \frac{N_A}{k_B}\left[\frac{{\mu_{\text{eff}}}^2}{3(T - \Theta_P)} + \frac{{\mu_B}^2}{\delta}\right]$$

where μ_{eff} is the effective magnetic moment, Θ_P is the Weiss constant, μ_B is the Bohr magneton, N_A is the Avogadro number and k_B is the Boltzmann constant. δ is an energy scale, which is defined as $\delta = 7\Delta E/20$ and describes the differences of the ground and excited states. The first term in the formula given above represents the Curie–Weiss susceptibility of the $J = 5/2$ ground state, while the second part represents the van Vleck susceptibility caused by the $J = 7/2$ multiplet, which is only slightly higher in energy.[88] Using the coefficients for the free ion values mentioned in the literature, this equation can be obtained from a more general one, which was published by Stewart.[91] It should be mentioned that both equations neglect crystal-field splitting of each J level and the mixture of one with another.

The fit obtained using the Hamaker equation given is shown in red in Fig. 17, top. The whole temperature region can be described very well, resulting in fit parameters of $\mu_{\text{eff}} = 0.61(1)\mu_B$, $\Theta_P = -0.3(1)$ K and $\delta = 468(5)$ K. The effective magnetic moment is slightly smaller than the $0.845\mu_B$ of the free ion for the $J = 5/2$ Hund's rule ground state of Sm^{3+}, $\delta = 468(5)$ K corresponds to $\Delta E = 1337$ K. The energy difference is slightly smaller compared to the ideal value of 1550 K, however, well in line with, *e.g.*, $SmPdGa_3$ ($\delta E = 471(5)$ K).[94] Interestingly, for ionic compounds, this energy barrier has not been determined at all to the best of our knowledge. However, 850 K is found for intermetallic $SmOs_4Sb_{12}$ [95] or 1080 K for $SmRh_4B_4$.[88]

For Eu^{3+} ($4f^6$, $S = 3$, $L = 3$) seven states of the multiplet ^7F_J exist with $^7F_0$ being the ground state. However, the sole contribution of the lowest state is only taken into account when a sufficiently large separation of the multiplet components (compared to k_BT) is present. For higher temperatures, the different components of the multiplet contribute and therefore have to be taken into account. The paramagnetic susceptibility can be expressed by the van Vleck theory:[93]

$$\chi_{\text{para}}(\text{free} > \text{Eu}^{3+}) = \frac{N{\mu_B}^2}{Z}\left(\frac{A}{3\lambda}\right) + n\left(\frac{C}{T}\right) + \chi_0.$$

The expressions of A and Z contain the contributions of the respective ground states found in the literature.[92] In order to describe the contributions of the trace Eu^{2+} and diamagnetic impurities, a C/T term and a χ_0 term have been added to the equation. The parameter λ describes the coupling constant. A fit of the magnetic susceptibility data is shown in Fig. 17, bottom. When neglecting the Eu^{2+} impurities, the fit plotted as a solid green line is obtained ($\lambda = 610(10)$ K, $\chi_0 = 4.8(1) \times 10^{-4}$ emu mol^{-1}). When adding the paramagnetic Eu^{2+} contributions, the fit represented by the red line is obtained and the parameters of $\lambda = 612(10)$ K, $n = 4(1) \times 10^{-4}$ and $\chi_0 = 5.6(1) \times 10^{-3}$ emu mol^{-1} resulted. The obtained χ_0 value agrees with[50] and the coupling constants are slightly elevated with respect to the value of $\lambda = 480$ K of a free Eu^{3+} ion or other ionic Eu^{3+} compounds in the literature (EuF_3:[92] $\lambda = 490$ K; $EuBO_3$:[92] $\lambda = 471$ K; $Eu_2Ta_2O_{7.1}N_{0.6}$:[96] $\lambda = 390(2)$ K; $Eu_2[B_2(SO_4)_6]$:[19] $\lambda = 589$ K). However, Bozorth and van Vleck already mentioned that the coupling constant in metallic Eu is lower than expected ($\lambda = 285$ K),[87] in line with significant hybridisation effects. Comparable values have been also observed in intermetallic $Eu_2Ir_3Al_9$ ($\lambda = 290(10)$ K).[89] Using the spectroscopic data discussed earlier, *i.e.* the energy values of the $^5D_1 \rightarrow {}^7F_0$ and $^5D_0 \rightarrow {}^7F_1$ transitions in the fluorescence spectrum (Fig. 11) and the $^7F_0 \rightarrow {}^5D_1$ and $^5D_0$ bands in the UV-Vis spectrum (Fig. S19†), an energy difference between the $^7F_0$ and $^7F_1$ states of 555 K could be calculated being in good agreement with the λ value of 612 K.

$Na_5Bi(WO_4)_4$ (Fig. S26h†) finally exhibits almost temperature independent diamagnetism, in line with all atoms being a close shell. However, this also proves that tungsten is in the oxidation state +6 with no unpaired electrons. The susceptibility at 300 K is $\chi(300\text{ K}) = -190(1) \times 10^{-6}$ emu mol^{-1}, which is in good agreement with the sum of the increment values of -303×10^{-6} emu mol^{-1} (individual values according to ref. 97: Na^+: -6.8×10^{-6} emu mol^{-1}; Bi^{3+}: -25×10^{-6} emu mol^{-1}; W^{6+}: -13×10^{-6} emu mol^{-1}, O^{2-}: -12×10^{-6} emu mol^{-1}). The Curie-like increase below *circa* 50 K is attributed to trace amounts of paramagnetic impurities.

^{151}Eu Mössbauer spectroscopy

The ^{151}Eu Mössbauer spectrum of $Na_5Eu(WO_4)_4$ is shown in Fig. 18. Only one spectral contribution with a line width of $\Gamma = 2.45(3)$ mm s^{-1} at a typical isomer shift for trivalent Eu at $\delta = +0.55(1)$ mm s^{-1} can be observed. The recently published

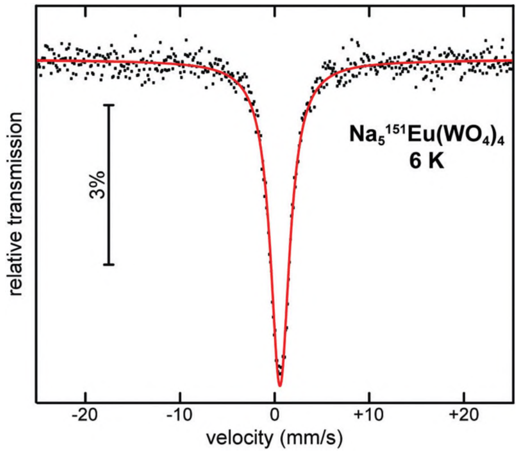

Fig. 18 Experimental (data points) and simulated (continuous line) ^{151}Eu Mössbauer spectra of $Na_5Eu(WO_4)_4$ measured at 6 K.

Mössbauer spectroscopic results of the tungstate $KEu(WO_4)_2$ show an almost identical isomer shift for the trivalent Eu atoms in that compound.[18] Due to the symmetric crystallographic environment of the Eu atoms the quadrupole splitting was kept fixed at $\Delta E_Q = 0$ mm s^{-1}.

Experimental section

Materials

La_2O_3 (99.99%), Ho_2O_3 (99.9%), Er_2O_3 (99.9%), Yb_2O_3 (99.9%) (all from Auer-Remy), CeO_2 (99.99%, MaTecK), Pr_6O_{11} (99.9%), Nd_2O_3 (99.9%), $Na_2WO_4{\cdot}2H_2O$ (99%, all from Merck), Sm_2O_3 (99.9%, MC Industrial Chemical), Eu_2O_3 (99.99%), Tb_4O_7 (99.9%), Dy_2O_3 (99.99%), Tm_2O_3 (99.9%), Lu_2O_3 (99.9%, all from Chempur), Gd_2O_3 (99.99%, Fluka), Bi_2O_3 (99.5%, Riedel-de Haën), Y_2O_3 (99.99%), WO_3 (99.8%, both from Alfa Aesar) and Na_2CO_3 (99%, AppliChem) were used as starting materials without further purification and were handled in air. The respective purities are given in parentheses.

Syntheses

Samples of the composition $Na_5M(WO_4)_4$ (M = La, Ce, Pr, Nd, Sm, Eu, Gd, Tb, Dy, Ho, Er, Tm, Yb, Lu, Y, Bi) were prepared *via* a flux synthesis. The starting materials were weighed in stoichiometric ratios following the reaction equation $\frac{1}{2}Na_2CO_3 + \frac{1}{2}M_2O_3 + 2WO_3 + 2Na_2WO_4{\cdot}2H_2O \rightarrow Na_5M(WO_4)_4 + \frac{1}{2}CO_2$ and the respective equations for CeO_2, Pr_6O_{11}, and Tb_4O_7 with an excess of 500% of $Na_2WO_4{\cdot}2H_2O$ as the flux. The ground powders were transferred into corundum crucibles and heated at 600 °C for 90 h in air inside a muffle furnace with heating ramps of 200 K h^{-1}. Subsequently, the obtained powders were dissolved in 50 ml hot deionized water (200 °C) under constant magnetic stirring (500 rpm) for 1 h, vacuum-filtered along with washing with an additional 50 ml of H_2O and dried in a compartment dryer at 65 °C for 24 h. The $Na_5Y_{1-x}Eu_x(WO_4)_4$ (x = 0.01, 0.05, 0.1, 0.5) and $Na_5Y_{1-y}Tb_y(WO_4)_4$ (y = 0.01, 0.02, 0.05, 0.5) samples were prepared in the same way combining appropriate amounts of the educts Y_2O_3 plus Eu_2O_3 and Y_2O_3 plus Tb_4O_7, respectively. Single crystals of $Na_5M(WO_4)_4$ (M = Ce, Pr, Nd, Sm, Eu, Gd, Tb, Ho, Tm, Yb, Bi) as well as of $Na_5Y_{0.5}Eu_{0.5}(WO_4)_4$ and $Na_5Y_{0.5}Tb_{0.5}(WO_4)_4$ were grown from the melt. The respective polycrystalline powders were heated in platinum crucibles inside a muffle furnace at 800 °C for 10 h with a heating ramp of 200 K h^{-1} and cooled to 400 °C with a ramp of 5 K h^{-1} and subsequently to room temperature with a ramp of 200 K h^{-1}. Alternatively, samples of $Na_5Y_{1-x}Eu_x(WO_4)_4$ (x = 0.5, 1) were prepared *via* two different solid state reactions. Firstly (Synthesis A1), stoichiometric amounts of the educts according to the reaction equation $\frac{1}{2}(1-x)Y_2O_3 + \frac{1}{2}xEu_2O_3 + 1.5WO_3 + 2.5Na_2WO_4{\cdot}2H_2O \rightarrow Na_5M(WO_4)_4$ reported by Chiu *et al.*[6] were ground and heated inside a muffle furnace in corundum crucibles at 600 °C for 6 h in air with heating ramps of 200 K h^{-1}. Subsequently, the same washing steps were carried out as for the flux synthesis. Secondly (Synthesis A2), the educts according to the reaction equation $2.5Na_2CO_3 + \frac{1}{2}(1-x)Y_2O_3 + \frac{1}{2}xEu_2O_3 + 4WO_3 + 2.5Na_2WO_4{\cdot}2H_2O \rightarrow Na_5Y_xEu_x(WO_4)_4 + 2.5CO_2$ reported by Huang *et al.*[30] were weighed in stoichiometric ratios, ground and transferred into corundum crucibles, which were heated at 700 °C for 6 h in air inside a muffle furnace with heating ramps of 200 K h^{-1}. Then, the same washing steps were carried out as for the molten salt synthesis. The choice of starting materials, *i.e.* choosing Na_2CO_3 or Na_2WO_4 as the sodium source, is expected to play only a minor role since van Vliet and Blasse report the synthesis of $Na_5Gd(WO_4)_4$ with the temperature program of A1 and the educts of A2.[36]

Additionally, polycrystalline $NaEu(WO_4)_2$ was prepared *via* a solid state reaction similar to the one reported by Wang *et al.*[45] according to the reaction equation $Na_2CO_3 + Eu_2O_3 + 4WO_3 \rightarrow 2NaEu(WO_4)_2 + CO_2$ weighing and subsequently grinding stoichiometric amounts of the educts with a surplus of 10% Na_2CO_3 due to losses caused by the evaporation of CO_2. The mixture was heated inside a muffle furnace in a corundum crucible at 800 °C for 10 h in air with heating ramps of 200 K h^{-1}. Single crystals of $NaEu(WO_4)_2$ were grown from the melt, heating polycrystalline $NaEu(WO_4)_2$ in a platinum crucible inside a muffle furnace in air at 1000 °C for 10 h with a heating ramp of 200 K h^{-1} and cooled to 400 °C with a ramp of 5 K h^{-1} and subsequently to room temperature with a ramp of 200 K h^{-1}.

Single crystal structure determination

Suitable single crystals were selected for single-crystal XRD under a polarising microscope. Diffraction data were collected with a Bruker D8 Venture diffractometer using Mo-K$_\alpha$ radiation (λ = 0.7093 Å). Absorption correction was performed by the multiscan method. The structures were solved by Direct Methods and refined by the full-matrix least-squares technique using the SHELXTL crystallographic software package.[98] Relevant crystallographic data and further details of the structure determinations are presented in Tables 1, S1, S2 and S11.†

Further details of the crystal structure investigations may be obtained from the Fachinformationszentrum Karlsruhe, 76344 Eggenstein-Leopoldshafen, Germany (Fax: +49-7247-808-666; E-mail: crysdata@fiz-karlsruhe.de, http://www.fiz-karlsruhe.de/request for deposited data.html) on quoting the depository numbers CSD 1986858 ($Na_5Bi(WO_4)_4$), 1986859 ($Na_5Pr(WO_4)_4$), 19868560 ($Na_5Y_{0.49}Tb_{0.51}(WO_4)_4$), 1986861 ($Na_5Tb(WO_4)_4$), 1986862 ($Na_5Sm(WO_4)_4$), 1986863 ($Na_5Tm(WO_4)_4$), 1986864 ($Na_5Y_{0.49}Eu_{0.51}(WO_4)_4$), 1986865 ($Na_5Eu(WO_4)_4$), 1986866 ($NaEu(WO_4)_2$), 1986867 ($Na_5Yb(WO_4)_4$), 1986868 ($Na_5Gd(WO_4)_4$), 1986869 ($Na_5Ho(WO_4)_4$), 1986870 ($Na_5Ce(WO_4)_4$), 1986871 ($Na_5Nd(WO_4)_4$) and 1986872 ($Na_5Dy(WO_4)_4$).†

X-ray powder diffraction and Rietveld refinement

Ground samples were prepared on a stainless steel sample holder and flattened using a glass plate. The X-ray powder diffraction patterns were recorded with a Seifert 3003 TT diffractometer at room temperature in Bragg–Brentano geometry using Cu-K$_\alpha$ radiation (λ = 1.54184 Å), a GE METEOR 1D line detector, and a Ni-filter to suppress K_β radiation (X-ray tube operated at 40 kV and 40 mA, scan range: 5–120°, increment: 0.01°, 40 scans per data point, integration time: 2500 s per degree, variable divergence slit). Analysis of the diffraction data was performed using the Rietveld method using the program TOPAS V. 5.0.[99] The instrumental resolution function was determined empirically from a set of fundamental parameters using a reference scan of Si (NIST 640d).[100] The structural model of $Na_5Ho(WO_4)_4$ from our single crystal XRD measurements was used as a starting model for Rietveld analysis of the respective $Na_5M(WO_4)_4$ samples. Additionally, the side phases of $NaM(WO_4)_2$ and Na_2WO_4 were refined starting from the structure of $NaDy(WO_4)_2$ reported by Zhao *et al.* (CSD 248012)[47] and Na_2WO_4 reported by Fortes (CSD 195519),[11] respectively. Isotropic displacement parameters were constrained to one common value for the heavy atoms (W, M) and another for the residual atoms (Na, O) in order to minimise quantification errors. Further details of the crystal structure investigations by Rietveld refinement may be obtained from the Fachinformationszentrum Karlsruhe, 76344 Eggenstein-Leopoldshafen, Germany (Fax: +49-7247-808-666; E-mail: crysdata@fiz-karlsruhe.de, http://www.fiz-karlsruhe.de/request for deposited data.html) on quoting the depository numbers CSD 1986873 ($Na_5Er(WO_4)_4$), 1986874 ($Na_5La(WO_4)_4$), 1986875 ($Na_5Y(WO_4)_4$) and 1986876 ($Na_5Lu(WO_4)_4$).†

Differential scanning calorimetry

The DSC measurements were performed with a NETZSCH STA 409 PC Luxx thermobalance under a N_2 atmosphere with 50 mL min^{-1} flow in platinum crucibles (heating rate: 10 K min^{-1}).

Variable-temperature X-ray powder diffraction

The samples were ground and filled into a silica-glass Hilgenberg glass capillary (outer diameter: 0.3 mm, wall thickness: 0.01 mm). The data were collected between T = 50 and 800 °C with a Bruker D8 Advance diffractometer with Cu-K_α radiation (λ = 1.54184 Å) with a 1D LynxEye detector, steps of 0.02°, acquisition time 5 s per step and transmission geometry (scan range: 10–65°, fixed divergence slit: 0.6 mm). The generator was driven at 40 kV and 40 mA.

FTIR spectroscopy

The Fourier-transform infrared spectra were recorded at room temperature with a Bruker EQUINOX 55 T-R spectrometer using a Platinum ATR device (scan range: 400–4000 cm^{-1}, resolution: 2 cm^{-1}, 32 scans per sample).

UV/Vis spectroscopy

The UV/Vis spectra were recorded as diffuse reflection spectra at room temperature with a Varian Cary 300 Scan UV/Vis spectrophotometer using an Ulbricht sphere detector and a deuterium lamp/mercury lamp light source (scan range: 200–800 nm, increment: 1 nm, scan rate: 120 nm cm^{-1}).

Fluorescence spectroscopy

Solid-state excitation and emission spectra were recorded on a Horiba FluoroMax-4 fluorescence spectrometer equipped with a xenon discharge lamp scanning a range from 200 to 800 nm. The excitation spectra were corrected with respect to the lamp intensity. Low temperature measurements were performed with a liquid nitrogen dewar assembly within the same device.

Magnetic properties

The powdered samples of the $Na_5M(WO_4)_4$ series with M = Ce, Pr, Sm, Eu, Tb, Tm, Yb and Bi were packed into polyethylene (PE) capsules and attached to the sample holder rod of a Vibrating Sample Magnetometer (VSM) for measuring the magnetisation $M(T, H)$ in a Quantum Design Physical Property Measurement System (PPMS). The samples were investigated in the temperature range of 2.5–300 K with applied external magnetic fields up to 80 kOe. The recorded susceptibilities were corrected for the diamagnetic contributions, calculated from the increments tabulated in ref. 97. For the rare-earth representatives χ_{dia} ($Na_5RE(WO_4)_4$) = -297×10^{-6} emu mol^{-1} ($= 5 \times -6.8 \times 10^{-6}$ emu mol^{-1} + $1 \times -19 \times 10^{-6}$ emu mol^{-1} + $4 \times -13 \times 10^{-6}$ emu mol^{-1} + $16 \times -12 \times 10^{-6}$ emu mol^{-1}) was calculated.

^{151}Eu Mössbauer spectroscopy

For the ^{151}Eu Mössbauer spectroscopic investigation of $Na_5Eu(WO_4)_4$ the 21.53 keV transition of a $^{151}Sm{:}EuF_3$ source (55 MBq, 1% of the total source activity) was used. The sample was cooled to 6 K in a continuous flow He-cryostat system (Janis Research Co. LLC) while the source was kept at room temperature. The experiment was conducted in the usual transmission geometry. The ideal absorber thickness was calculated according to the work of Long *et al.*[101] The transmission integral fits were obtained using the WinNormos for Igor6 program package.[102]

Conclusions

In this extensive systematic study, the pentasodium rare earth tetratungstates $Na_5M(WO_4)_4$ (M = Y, La–Nd, Sm–Lu, Bi) are investigated over the whole range of M^{3+} ions with respect to crystal structure, crystallographic relationships and thermal, magnetic, ^{151}Eu Mössbauer spectroscopic and optical properties. Firstly, the flux syntheses of $Na_5M(WO_4)_4$ (M = La–Nd, Sm–Lu, Y, Bi) with a surplus of 500% Na_2WO_4 yield significantly smaller amounts of the $NaM(WO_4)_2$ side phases compared to simple solid state reactions. The first reports of the structures of $Na_5M(WO_4)_4$ (M = Ce, Pr, Sm, Dy, Ho, Er, Tm, Yb, Bi) and the first reports from single-crystal data for $NaEu(WO_4)_2$ and $Na_5Eu(WO_4)_4$ are given alongside the remaining $Na_5M(WO_4)_4$ crystal structures. The crystallographic relationship of $Na_5M(WO_4)_4$ to $NaM(WO_4)_2$ is described by a group–subgroup relation. This explains the competitive crystallisation of both compounds. Furthermore, $Na_5M(WO_4)_4$ decomposes while simultaneously melting to $NaM(WO_4)_2$ and

Na_2WO_4. There is a maximum in the melting and decomposition temperature for $Na_5Ho(WO_4)_4$. This can be explained by the ionic radii difference $|r(M) - r(Na)|$ in $Na_5M(WO_4)_4$ determining the energy benefit of the disorder in $NaM(WO_4)_2$ after the decomposition taking into account the existence of domains within the crystal structure related to the decomposition products, a behaviour also known as chemical twinning.

$Na_5M(WO_4)_4$ is a promising class of phosphors due to the possible O^{2-}–W^{6+} LMCT excitation and the large M–M distances yielding special properties like the lack of concentration quenching or the absence of cross relaxation of neighbouring Sm^{3+} ions. Fluorescence spectroscopy on $Na_5M(WO_4)_4$ (M = Pr, Sm, Eu, Tb, Tm, Bi), $Na_5Y_{1-x}Eu_x(WO_4)_4$ and $Na_5Y_{1-y}Tb_y(WO_4)_4$ showed – besides the weak coordination – that the energy transfer from ${WO_4}^{2-}$ to M^{3+} is governed by the W^{6+}–O^{2-} LMCT emission.

Furthermore, we identified and characterised the temperature dependent miscibility gap in $Na_5Y_{1-x}Eu_x(WO_4)_4$ and $Na_5Y_{1-y}Tb_y(WO_4)_4$. Solid solutions are formed irreversibly above a threshold temperature of 660 °C to 700 °C.

Finally, the temperature dependent measurement of the magnetic susceptibility of $Na_5M(WO_4)_4$ (M = Ce, Pr, Sm, Eu, Tb, Tm, Yb, Bi) showed no onset of any magnetic interactions in agreement with the large M–M distances. The oxidation states +6 of tungsten and +3 of M were confirmed by the magnetic properties of $Na_5Bi(WO_4)_4$ and the ^{151}Eu Mössbauer spectrum of $Na_5Eu(WO_4)_4$, respectively.

Conflicts of interest

There are no conflicts to declare.

References

1 S. G. Jantz, F. Pielnhofer, M. Dialer and H. A. Höppe, *Z. Anorg. Allg. Chem.*, 2017, **643**, 2024–2030.
2 S. G. Jantz, F. Pielnhofer, M. Dialer and H. A. Höppe, *Z. Anorg. Allg. Chem.*, 2017, **643**, 2031–2037.
3 M. Daub, A. J. Lehner and H. A. Höppe, *Dalton Trans.*, 2012, **41**, 12121–12128.
4 T. Schustereit, P. Netzsch, H. A. Höppe and I. Hartenbach, *Z. Anorg. Allg. Chem.*, 2018, **101**, 11.
5 R. F. Klevtsova, L. Glinskaya, L. P. Kozeeva and P. V. Klevtsov, *Crystallogr. Rep.*, 1972, **17**, 672–676.
6 C.-H. Chiu, C.-H. Liu, S.-B. Huang and T.-M. Chen, *J. Electrochem. Soc.*, 2008, **155**, J71–J77.
7 J. Liao, B. Qiu, H. Wen, J. Chen, W. You and L. Liu, *J. Alloys Compd.*, 2009, **487**, 758–762.
8 J. Liao, B. Qiu and H. Lai, *J. Lumin.*, 2009, **129**, 668–671.
9 J. Liao, S. Zhang, H. You, H.-R. Wen, J.-L. Chen and W. You, *Opt. Mater.*, 2011, **33**, 953–957.
10 Y. Liu, G. Liu, J. Wang, X. Dong and W. Yu, *Inorg. Chem.*, 2014, **53**, 11457–11466.
11 A. D. Fortes, *Acta Crystallogr., Sect. E: Crystallogr. Commun.*, 2015, **71**, 592–596.
12 F. B. Xiong, Z. W. Zhang, H. F. Lin, L. J. Wang, Y. C. Xu and W. Z. Zhu, *Opt. Mater.*, 2015, **42**, 394–398.
13 A. Durairajan, D. Thangaraju, M. Valente and S. Moorthy Babu, *J. Electron. Mater.*, 2015, **44**, 4199–4206.
14 A. Durairajan, D. Balaji, K. Kavi Rasu, S. Moorthy Babu, M. A. Valente, D. Thangaraju and Y. Hayakawa, *J. Lumin.*, 2016, **170**, 743–748.
15 J. Kim, *Inorg. Chem.*, 2017, **56**, 8078–8086.
16 J. Han, F. Pan, M. S. Molokeev, J. Dai, M. Peng, W. Zhou and J. Wang, *ACS Appl. Mater. Interfaces*, 2018, **10**, 13660–13668.
17 X. Wang, X. Shi, M. S. Molokeev, Z. Wang, Q. Zhu, X. Li, X. Sun and J.-G. Li, *Inorg. Chem.*, 2018, **57**, 13606–13617.
18 P. Pues, S. Schwung, D. Rytz, L. Schubert, S. Klenner, F. Stegemann, R. Pöttgen and T. Jüstel, *J. Lumin.*, 2019, **215**, 116653.
19 P. Netzsch, M. Hämmer, P. Gross, H. Bariss, T. Block, L. Heletta, R. Pöttgen, J. Bruns, H. Huppertz and H. A. Höppe, *Dalton Trans.*, 2019, **48**, 4387–4397.
20 P. Netzsch, P. Gross, H. Takahashi, S. Lotfi, J. Brgoch and H. A. Höppe, *Eur. J. Inorg. Chem.*, 2019, 3975–3981.
21 S. G. Jantz, F. Pielnhofer, L. van Wüllen, R. Weihrich, M. J. Schäfer and H. A. Höppe, *Chem. – Eur. J.*, 2018, **24**, 443–450.
22 S. G. Jantz, M. Dialer, L. Bayarjargal, B. Winkler, L. van Wüllen, F. Pielnhofer, J. Brgoch, R. Weihrich and H. A. Höppe, *Adv. Opt. Mater.*, 2018, **7**, 1800497.
23 K. Förg and H. A. Höppe, *Dalton Trans.*, 2015, **44**, 19163–19174.
24 H. A. Höppe, *J. Solid State Chem.*, 2009, **182**, 1786–1791.
25 L. G. Sillén and H. Sundvall, *Ark. Kemi, Mineral. Geol.*, 1943, **17A**, 1–8.
26 H.-P. Hong and K. Dwight, *Mater. Res. Bull.*, 1974, **9**, 775–780.
27 V. A. Efremov, V. K. Trunov and T. A. Berezina, *Kristallografiya*, 1982, **27**, 134–139.
28 L. Yao, *Zhongguo Jiguang*, 1989, **16**, 123–125.
29 I. Hartenbach, B. Marchetti and T. Schleid, *Z. Kristallogr. Suppl. Issue*, 2007, **25**, 22.
30 D. C. Huang, Y. F. Zhou, W. T. Xu, Z. F. Yang, M. C. Hong, Y. H. Lin and J. C. Yu, *Adv. Mater. Res.*, 2012, **624**, 244–247.
31 G. Q. Wang, Y. P. Lin, R. Ye, Y. N. Feng and L. Y. Li, *J. Alloys Compd.*, 2019, **779**, 41–48.
32 C. Guo, F. Gao, Y. Xu, L. Liang, F. G. Shi and B. Yan, *J. Phys. D: Appl. Phys.*, 2009, **42**, 095407.
33 D. Qin and W. Tang, *RSC Adv.*, 2016, **6**, 45376–45385.
34 D. Huang, Y. Zhou, W. Xu, Z. Yang, Z. Liu, M. Hong, Y. Lin and J. Yu, *J. Alloys Compd.*, 2013, **554**, 312–318.
35 J. Pan, L. Yau, L. Chen, G. Zhao, G. Zhou and C. Guo, *J. Lumin.*, 1988, **40–41**, 856–857.

36 J. van Vliet and G. Blasse, *J. Solid State Chem.*, 1990, **85**, 56–64.

37 H. Höppe, *Angew. Chem.*, 2009, **121**, 3626–3636.

38 H. Höppe, *Angew. Chem., Int. Ed.*, 2009, **48**, 3572–3582.

39 Z. Xia and Q. Liu, *Prog. Mater. Sci.*, 2016, **84**, 59–117.

40 G. Blasse and A. Bril, *J. Chem. Phys.*, 1966, **45**, 2350–2355.

41 S. I. Weissman, *J. Chem. Phys.*, 1942, **10**, 214–217.

42 N. Saito, N. Sonoyama and T. Sakata, *Bull. Chem. Soc. Jpn.*, 1996, **69**, 2191–2194.

43 D. Huang, Y. Zhou, W. Xu, Z. Yang, M. Hong and J. Yu, *J. Lumin.*, 2012, **132**, 2788–2793.

44 J. Zhang, Z. Q. Chen, C. H. Wang, A. M. Li, H. Yin and Z. Li, *Adv. Mater. Res.*, 2013, **787**, 281–285.

45 H. Wang, Y. Li, Z. Ning, L. Huang, C. Zhong, C. Wang, M. Liu, X. Lai, D. Gao and J. Bi, *J. Lumin.*, 2018, **201**, 364–371.

46 N. J. Stedman, A. K. Cheetham and P. D. Battle, *J. Mater. Chem.*, 1994, **4**, 707.

47 D. Zhao, F. Li, W. Cheng and H. Zhang, *Acta Crystallogr., Sect. E: Struct. Rep. Online*, 2009, **66**, i2.

48 H. Bärnighausen, *MATCH Commun. Math. Comput. Chem.*, 1980, **9**, 139–175.

49 U. Müller, *Z. Anorg. Allg. Chem.*, 2004, **630**, 1519–1537.

50 J. Huang, J. Loriers, P. Porcher, G. Teste de Sagey, P. Caro and C. Levy-Clement, *J. Chem. Phys.*, 1984, **80**, 6204–6209.

51 R. D. Shannon, *Acta Crystallogr., Sect. A: Cryst. Phys., Diffr., Theor. Gen. Crystallogr.*, 1976, **32**, 751–767.

52 T. Balić Žunić and E. Makovicky, *Acta Crystallogr., Sect. B: Struct. Sci.*, 1996, **52**, 78–81.

53 E. Makovicky and T. Balić-Žunić, *Acta Crystallogr., Sect. B: Struct. Sci.*, 1998, **54**, 766–773.

54 R. Hoppe, *Angew. Chem.*, 1966, **78**, 52–63.

55 R. Hoppe, *Angew. Chem., Int. Ed.*, 1970, **9**, 25–34.

56 R. Hübenthal, *MAPLE: Program for the Calculation of the Madelung Part of Lattice Energy*, 1993.

57 A. Saiki, N. Ishizawa, N. Mizutani and M. Kato, *J. Ceram. Assoc. Jpn.*, 1985, **93**, 649–654.

58 E. Zintl, A. Harder and B. Dauth, *Z. Elektrochem. Angew. Phys. Chem.*, 1934, **40**, 558–593.

59 G. Schiller, Dissertation, Universität Karlsruhe, 1985.

60 A. Aird, M. C. Domeneghetti, F. Mazzi, V. Tazzoli and E. K. H. Salje, *J. Phys.: Condens. Matter*, 1998, **10**, L569–L574.

61 H. C. R. Wolf and R. Hoppe, *Z. Anorg. Allg. Chem.*, 1985, **529**, 61–64.

62 M. Gasgnier, G. Schiffmacher, P. Caro and L. Eyring, *J. Less-Common Met.*, 1986, **116**, 31–42.

63 B. Antic, M. Mitric and D. Rodic, *J. Magn. Magn. Mater.*, 1995, **145**, 349–356.

64 T. Schleid and G. Meyer, *J. Less-Common Met.*, 1989, **149**, 73–80.

65 S. Hull, S. T. Norberg, M. G. Tucker, S. G. Eriksson, C. E. Mohn and S. Stølen, *Dalton Trans.*, 2009, 8737–8745.

66 S. Seidel and R. Pöttgen, *Z. Kristallogr.*, 2020, **235**, 29–39.

67 L. Vegard, *Z. Phys.*, 1921, **5**, 17–26.

68 N. T. McDevitt and W. L. Baun, *Spectrochim. Acta*, 1964, **20**, 799–808.

69 *Phosphor handbook*, ed. H. Yamamoto, S. Shionoya and W. M. Yen, Taylor & Francis distributor, Boca Raton, FL and London, 2nd edn, 2007.

70 W. T. Carnall, P. R. Fields and K. Rajnak, *J. Chem. Phys.*, 1968, **49**, 4424–4442.

71 W. T. Carnall, P. R. Fields and B. G. Wybourne, *J. Chem. Phys.*, 1965, **42**, 3797–3806.

72 W. T. Carnall, P. R. Fields and K. Rajnak, *J. Chem. Phys.*, 1968, **49**, 4450–4455.

73 K. Kazmierczak and H. A. Höppe, *J. Solid State Chem.*, 2011, **184**, 1221–1226.

74 H. A. Höppe, G. Kotzyba, R. Pöttgen and W. Schnick, *J. Mater. Chem.*, 2001, **11**, 3300–3306.

75 D. L. Dexter, *J. Chem. Phys.*, 1953, **21**, 836–850.

76 T. Förster, *Z. Elektrochem.*, 1949, **53**, 93–99.

77 T. Förster, *Radiat. Res., Suppl.*, 1960, **2**, 326.

78 P. Boutinaud, R. Mahiou, E. Cavalli and M. Bettinelli, *J. Lumin.*, 2007, **122–123**, 430–433.

79 E. Pinel, P. Boutinaud and R. Mahiou, *J. Alloys Compd.*, 2004, **374**, 165–168.

80 P. Boutinaud, M. Bettinelli and F. Diaz, *Opt. Mater.*, 2010, **32**, 1659–1663.

81 K. Li and R. van Deun, *Dalton Trans.*, 2018, **47**, 6995–7004.

82 G. Blasse, *J. Solid State Chem.*, 1972, **4**, 52–54.

83 K. Binnemans, *Coord. Chem. Rev.*, 2015, **295**, 1–45.

84 H. E. Hoefdraad, *J. Solid State Chem.*, 1975, **15**, 175–177.

85 P. Dorenbos, *J. Lumin.*, 2005, **111**, 89–104.

86 W. T. Carnall, P. R. Fields and K. Rajnak, *J. Chem. Phys.*, 1968, **49**, 4447–4449.

87 R. M. Bozorth and J. H. van Vleck, *Phys. Rev.*, 1960, **118**, 1493–1498.

88 H. C. Hamaker, L. D. Woolf, H. B. MacKay, Z. Fisk and M. B. Maple, *Solid State Commun.*, 1979, **32**, 289–294.

89 F. Stegemann, T. Block, S. Klenner and O. Janka, *Chem. – Eur. J*, 2019, **25**, 3505–3509.

90 A. M. Stewart, *Phys. Rev. B: Solid State*, 1972, **6**, 1985–1998.

91 A. M. Stewart, *Phys. Rev. B: Condens. Matter Mater. Phys.*, 1993, **47**, 11242–11246.

92 Y. Takikawa, S. Ebisu and S. Nagata, *J. Phys. Chem. Solids*, 2010, **71**, 1592–1598.

93 J. H. van Vleck, *The Theory Of Electric And Magnetic Susceptibilities*, Oxford At The Clarendon Press, 1932.

94 S. Seidel, O. Niehaus, S. F. Matar, O. Janka, B. Gerke, U. C. Rodewald and R. Pöttgen, *Z. Naturforsch., B: J. Chem. Sci.*, 2014, **69**, 1105–1118.

95 W. M. Yuhasz, N. A. Frederick, P.-C. Ho, N. P. Butch, B. J. Taylor, T. A. Sayles, M. B. Maple, J. B. Betts, A. H. Lacerda, P. Rogl and G. Giester, *Phys. Rev. B: Condens. Matter Mater. Phys.*, 2005, **71**, 826.

96 B. Anke, S. Hund, C. Lorent, O. Janka, T. Block, R. Pöttgen and M. Lerch, *Z. Anorg. Allg. Chem.*, 2017, **643**, 1824–1830.

97 G. A. Bain and J. F. Berry, *J. Chem. Educ.*, 2008, **85**, 532.

98 G. M. Sheldrick, *Acta Crystallogr., Sect. C: Struct. Chem.*, 2015, **71**, 3–8.

99 Bruker AXS, *Topas V5, General profile and structure analysis software for powder diffraction data, User's Manual*, 2014.

100 R. W. Cheary, A. A. Coelho and J. P. Cline, *J. Res. Natl. Inst. Stand. Technol.*, 2004, **109**, 1–25.

101 G. J. Long, T. E. Cranshaw and G. Langsworth, *Moessbauer Eff. Ref. Data J.*, 1983, **216**, 42–49.

102 R. A. Brand, *WINNORMOS for IGOR6, version for IGOR6.2 or above: 22.07.2017*, 2017.